# Description and evaluation of the tropospheric aerosol scheme in the Integrated Forecasting System (IFS-AER, cycle 47R1) of ECMWF

Samuel Rémy[1], Zak Kipling[2], Vincent Huijnen[3], Johannes Flemming[2], Pierre Nabat[4], Martine Michou[4], Melanie Ades[2], Richard Engelen[2], and Vincent-Henri Peuch[2]

[1]HYGEOS, Lille, France
[2]European Centre for Medium Range Weather Forecasts, Reading, UK
[3]Royal Netherlands Meteorological Institute, De Bilt, Netherlands
[4]Météo-France, Toulouse, France

*Correspondence to:* Samuel Rémy (sr@hygeos.com)

**Abstract.**

   This article describes the IFS-AER aerosol scheme used operationally in the Integrated Forecasting System (IFS) cycle 47R1, operated by the European Centre for Medium Range Weather Forecasts (ECMWF) in the framework of the Copernicus Atmospheric Monitoring Services (CAMS). It represents an update of the Rémy et al. (2019) article which focused on cycle 45R1 of IFS-AER. The parameterizations of sources and sinks that have been updated since cycle 45R1 are described, as well as changes in the configuration used operationally within CAMS. As compared to cycle 45R1, a greater integration of aerosol and chemistry has been achieved. Primary aerosol sources have been updated, with the implementation of new dust and sea-salt aerosol emission schemes. New dry and wet deposition parameterizations have also been implemented. Sulfate production rates are now provided by the global chemistry component of the IFS. This paper aims to describe most of the updates that have been implemented since cycle 45R1 and not only the ones that are used operationally in cycle 47R1; components that are not used operationally will be clearly flagged.

   Cycle 47R1 of IFS-AER has been evaluated against a wide range surface and total column observations. The final simulated products such as Particulate Matter (PM) and Aerosol Optical Depth (AOD) generally show a significant increase in skill as compared to results obtained with cycle 45R1. Similarly, the simulated surface concentration of sulphate, organic matter and sea-salt aerosol is improved by cycle 47R1 as compared to cycle 45R1. Some imbalances persist, such as a too high surface concentration of nitrate and organic matter. The new wet and dry deposition schemes that have been implemented into cycle 47R1 have a mostly positive impact on simulated AOD, PM and speciated aerosol surface concentration.

## 1 Introduction

The Copernicus Atmosphere Monitoring Service (CAMS), operated by the ECMWF on behalf of the European Commission, provides operationally since 2014 Near-Real-Time twice daily global analyses and 5-day forecasts of aerosols, trace gases and green-house gases. It also released in September 2018 the CAMS reanalysis of atmospheric composition (Inness et al. (2019)), which has been continually updated since then and now covers 2003 to 2020. These global analyses and forecasts are provided by ECMWF's Integrated Forecasting System (IFS), which combines state-of-the-art meteorological and atmospheric composition modelling together with the data assimilation of satellite products. The IFS with atmospheric composition extensions has been first developed in the framework of the Global and regional Earth-system Monitoring using Satellite and in situ data project (GEMS; 2005 to 2009; Hollingsworth et al. (2008)), then during the Monitoring Atmospheric Composition and Climate series of projects (MACC, MACC-II, and MACC-III; 2010 to 2014) and finally during CAMS (2014 to present).The IFS is originally a numerical weather prediction system dedicated to operational meteorological forecasts. It was extended to forecast and assimilate aerosols (Morcrette et al. (2009), Benedetti et al. (2009), Rémy et al. (2019)), greenhouse gases (Engelen et al. (2009), Agustí-Panareda et al. (2014)), tropospheric reactive trace gases (Flemming et al. (2009), Flemming et al. (2015), Huijnen et al. (2016)) as well as stratospheric reactive gases (Huijnen et al. (2016)). "IFS-AER" denotes the IFS extended with the bin–bulk aerosol scheme used to provide global aerosol products in the CAMS project.

The parameterizations of IFS-AER cycle 38R2 and cycle 45R1 have been extensively described in Morcrette et al. (2009) and Rémy et al. (2019). Here, we aim to describe the updates of IFS-AER that have been implemented since cycle 45R1. Most of these updates are used in the version of cycle 47R1 used for operational forecasts, with the exception of the new dry and wet deposition schemes which for technical reasons were not included operationally and are expected to be part of operational cycle CY47R3. One year of cycling forecasts without data assimilation using cycle 45R1 and 47R1 IFS-AER have been evaluated against an extensive set of ground and remote sensing observational datasets.

Section 1 recalls the main characteristics of IFS-AER as well as its coupling to the operational global chemistry scheme IFS-CB05. Section 2 details the current and past operational configurations. Section 3 details the changes since cycle 45R1 in the representation of aerosol sources, and presents a few selected evaluation results. Section 4 presents the upgrade of the aerosol wet and dry deposition. Section 5 presents simulation results and budgets; Section 6 is dedicated to the global evaluation of cycle 45R1 and 47R1 IFS-AER simulations against remote sensing products and ground observations.

## 2 Main characteristics of IFS-AER

IFS-AER is a bulk–bin scheme derived from the LOA/LMDZ model (Boucher et al. (2002); Reddy et al. (2005)) using mass mixing ratio as the prognostic variable of the aerosol tracers. The aerosol species and the assumed size distribution are shown in Table 1; as compared to Rémy et al. (2019), only the nitrate and ammonium species differ. Since the implementation of operational cycle 46R1 in July 2019, the prognostic species are sea salt, desert dust, organic matter (OM), black carbon (BC), sulfate, nitrate and ammonium. IFS-AER is run by default coupled with the operational IFS-CB05 chemistry scheme; nevertheless it can also be run in stand-alone mode, i.e. without any interaction with the chemistry, in which case, the nitrate

and ammonium species are not included, and a specific tracer representing sulfur dioxide is added, as described in Rémy et al. (2019).

Desert dust is represented with three size bins, with radius bin limits at 0.03, 0.55, 0.9, and 20 μm). Sea salt aerosol is also represented with three size bins with radius bin limits of 0.03, 0.5, 5, and 20 μm at 80% relative humidity. All of sea-salt

5  aerosol parameters (concentration, emission, deposition) are expressed at 80% relative humidity, in contrast to the other aerosol species in IFS-AER, which are expressed as dry mixing ratio. The sea salt aerosol mass mixing ratio, emissions, etc. needs to be divided by a factor of 4.3 to convert to dry mass mixing ratio in order to account for the hygroscopic growth and change in density. For both dust and sea salt, there is no mass transfer between bins.

The organic matter and black carbon species consist of their hydrophilic and hydrophobic fractions, with the ageing processes

10 transferring mass from hydrophobic to hydrophilic component. Sulfate aerosols and, when not fully coupled to IFS-CB05, its precursor gas sulfur dioxide are represented by one prognostic variable each. When running fully coupled with IFS-CB05, which is the operational configuration since cycle 46R1, sulfur dioxide is represented in CB05 and thus not in IFS-AER. Since cycle 46R1, two extra species, nitrate and ammonium, are included in the operational products. The nitrate species consists of two prognostic variables that represent fine nitrate produced by gas–particle partitioning and coarse nitrate produced by

15 heterogeneous reactions of dust and sea salt particles. In all, IFS-AER is thus composed of 12 prognostic variables when running stand-alone and 14 when fully coupled with IFS-CB05 (including nitrates and ammonium), which allows for a relatively limited consumption of computing resources.

## 2.1 Coupling to the chemistry

One of the most important features of cycle 47R1 IFS-AER is its increasing integration of aerosol and chemistry. The sulfur and

20 nitrogen cycles are now represented across IFS-AER and IFS-CB05, and IFS-AER provides supplementary input to IFS-CB05 in order to better represent heterogeneous reactions as well as the impact of aerosols and photolysis rates.

### 2.1.1 sulfur cycle

The simplistic representation of the conversion of sulfur dioxide into sulfate aerosol used operationally in cycle 45R1 IFS-AER (Rémy et al. (2019)) has been replaced by a full coupling to the chemistry whereby the sulfate production rates are computed

25 and provided by IFS-CB05. This impacts most aspects of the simulated sulfur cycle, as shown by Table 2 and 3. The sulfur dioxide sources are slightly different: emissions from MACCity (Granier et al. (2011)) are used for the tracer included in standalone IFS-AER, while the more recent CAMS_GLOB_ANT (Granier et al. (2019)) are used for the sulfur dioxide tracer of IFS-CB05. The wet deposition of sulfur dioxide is represented in IFS-CB05 and not in the standalone version of IFS-AER, which adds an important sinks to the simulated sulfur dioxide. Finally, the chemical conversion rates are globally of the same

30 order of magnitude, but with large regional and vertical differences, leading to a much longer simulated lifetime of sulfur dioxide with cycle 47R1. There are no direct sulfate emissions in IFS-AER.

As shown in Table 3, the global budget of sulfate aerosol differs relatively little between CY45R1 and CY47R1, taking into account the fact that a new wet deposition routine is available in CY47R1, which will be detailed in section 4. However, the

**Table 1.** Aerosol species and parameters of the size distribution associated to each aerosol type in IFS-AER ($r_{\mathrm{mod}}$ =mode radius, $\rho$=particle density, $\sigma$=geometric standard deviation). **Values are for the dry aerosol apart from sea salt which is given at 80% RH.**

| Aerosol type | Size bin limits (sphere radius, $\mu$m) | $\rho$ (kg m$^{-3}$) | $r_{\mathrm{mod}}$ ($\mu$m) | $\sigma$ |
|---|---|---|---|---|
| Sea Salt (80% RH) | 0.03-0.5 0.5-5.0 5.0-20 | 1183 | 0.1992,1.992 | 1.9,2.0 |
| Dust | 0.03-0.55 0.55-0.9 0.9-20 | 2610 | 0.29 | 2.0 |
| Black carbon | 0.005-0.5 | 1000 | 0.0118 | 2.0 |
| Organic matter | 0.005-20 | 2000 | 0.021 | 2.24 |
| Sulfates | 0.005-20 | 1760 | 0.0355 | 2.0 |
| Nitrate fine | 0.03-0.9 | 1730 | 0.0355 | 2.0 |
| Nitrate coarse | 0.9-20 | 1400 | 0.199,1.992 | 1.9,2.0 |
| Ammonium | 0.005-20 | 1760 | 0.0355 | 2.0 |

**Table 2.** 2017 Global budget of sulfur dioxide as simulated by IFS. For cycle 45R1, the values from the sulfur dioxide tracer included in IFS-AER are shown. For cycle 47R1, the values from sulfur dioxide tracer of IFS-CB05 are shown. Fluxes are expressed in $TgS.yr^{-1}$ and burden in TgS.

| IFS-AER version | emissions | chemical conversion | dry deposition | wet deposition | burden | lifetime (days) |
|---|---|---|---|---|---|---|
| 45R1 | 70.3 | 42.9 | 27.4 | 0 | 0.11 | 0.57 |
| 47R1 | 73.8 | 41.4 | 19.9 | 12.3 | 0.68 | 3.36 |

**Table 3.** 2017 Global budget of sulfate aerosol as simulated by IFS-AER. Fluxes are expressed in $TgS.yr^{-1}$ and burden in TgS.

| IFS-AER version | emissions | chemical conversion | dry deposition | wet deposition | burden | lifetime (days) |
|---|---|---|---|---|---|---|
| 45R1 | 0. | 42.9 | 7.1 | 35.6 | 0.357 | 3.03 |
| 47R1 | 0. | 41.4 | 1.9 | 39.7 | 0.367 | 3.24 |

**Table 4.** 2017 Global budget of nitrate aerosol from gas/particle partitioning and from heterogeneous reactions, and of ammonium aerosol as simulated by IFS-AER. Fluxes are expressed in

| species | production | dry deposition | wet deposition | burden | lifetime (days) |
|---|---|---|---|---|---|
| Nitrate from gas/particle partitioning | 9.1 | 1.1 | 8. | 0.11 | 4.21 |
| Nitrate from heterogeneous reactions | 14.3 | 5.3 | 9.0 | 0.08 | 2.04 |
| Total particulate nitrate | 23.4 (13.5) | 6.4 (3.4) | 17. (10.1) | 0.19 (0.14) | 2.96 (3.78) |
| Ammonium | 14.5 (24.9) | 1.1 (4.5) | 13.5 (20.4) | 0.12 (0.23) | 3.02 (3.37) |

impact on simulated sulfate surface concentration is significant as shown by Figures 1 and 2. Over the U.S., sulfate is much overestimated by CY45R1 IFS-AER at surface against observations; this positive bias is largely eliminated with CY47R1. Over Europe, the improvement is less clear; but the trend towards lower simulated sulfate aerosol at surface is the same with CY47R1.

5 ### 2.1.2 Nitrate/ammonium

The production scheme of nitrate and ammonium through gas/particle partitioning processes, and of nitrate from heterogeneous reactions on dust and sea-salt particles, is detailed in Rémy et al. (2019). These two schemes use as input meteorological parameters provided by the IFS as well as the gaseous precursors: nitric acid and ammonia. The mass mixing ratios of these two are passed from IFS-CB05 to IFS-AER, used in the nitrate and ammonium production schemes, and updated in return by 10 those schemes. Table 4 shows the budget of the two nitrate species, total particulate nitrate and ammonium, comparing with the median values from the AEROCOM phase III experiment(Bian et al. (2017)). The comparison to values provided by Bian et al. (2017) can only be qualitative, because the emission of the precursor gases (ammonia, nitrous oxides) are different, and the years simulated are also not the same. However, the fact that no major disagreement appears shows that values simulated by IFS-AER fall in the range of values simulated by other models.
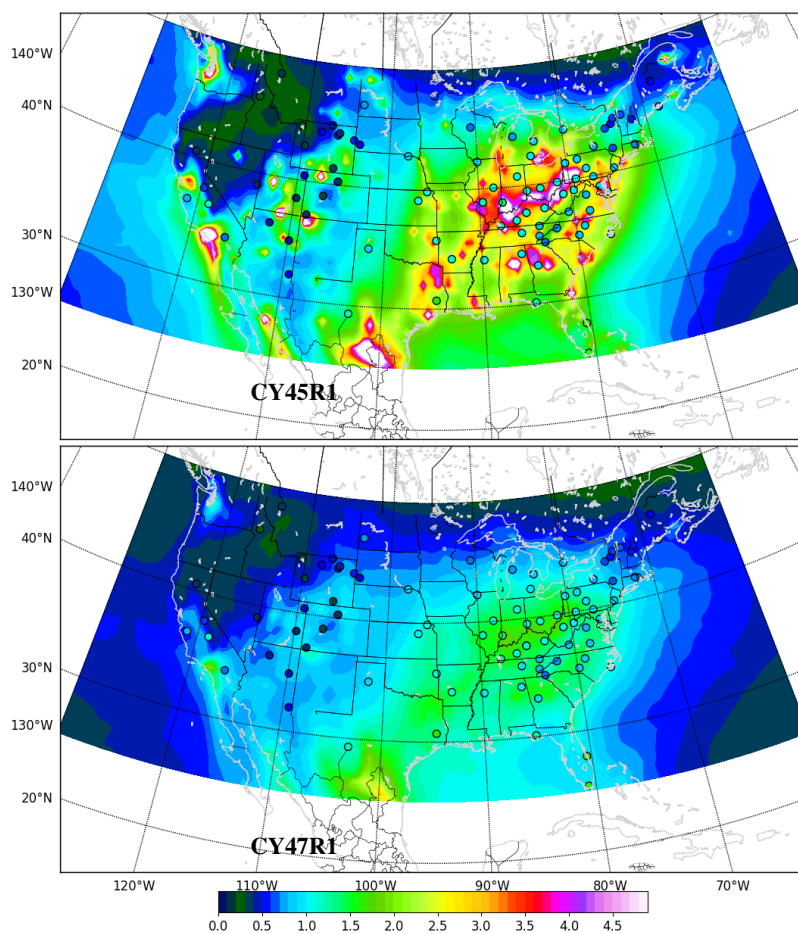
**Figure 1.** 2017 surface sulfate concentration in $\mu g/m^3$ simulated by IFS-AER CY45R1 (top) and CY47R1 (bottom) against yearly average from the CASTNET network, as shown in black circles.

## 2.2   Use of aerosol inputs in IFS-CB05

The global chemistry module of the IFS, IFS-CB05, uses aerosol mass mixing ratio input from IFS-AER to estimate the reaction rates of heterogeneous reactions on top of aerosol particles. The simulated Absorption Aerosol Optical Depth (AAOD) from IFS-AER also intervenes in the computation of photolysis rates Huijnen et al. (2016).
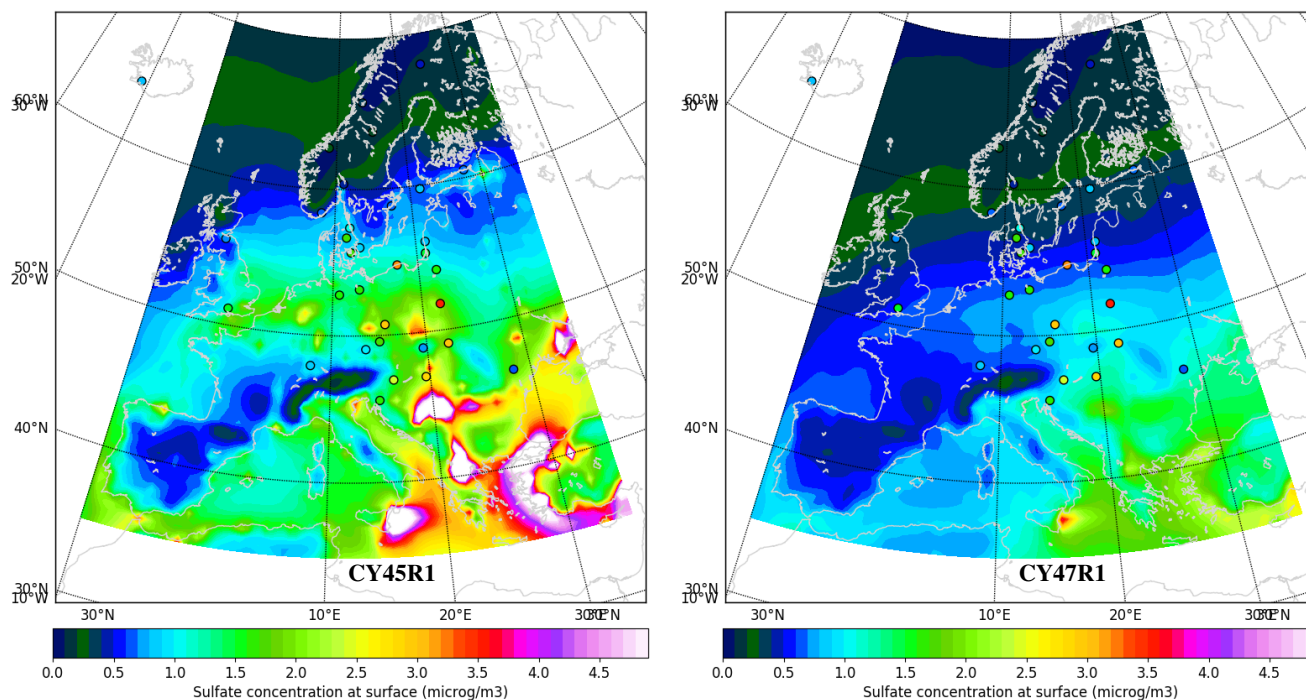
**Figure 2.** 2017 surface sulfate concentration in $\mu g/m^3$ simulated by IFS-AER CY45R1 (left) and CY47R1 (right) against yearly average from the EMEP network, as shown in black circles.

## 3 Operational configuration

IFS-AER cycle 47R1 was used operationally to provide Near-Real-Time (NRT) aerosol products within CAMS from October 2020 until May 2021, when the new cycle 47R2 became operational. The operational cycle 47R2 doesn't include any update of IFS-AER; the only feature that impacts simulated aerosol fields, besides the upgrade of the meteorological model, is the

5   implementation of a cap on primary OM emissions. More details on the implementation of cycle 47R2 can be found at https://confluence.ecmwf.int/display/COPSRV/Implementation+of+IFS+cycle+47r2. The operational cycle 47R2 also runs using single precision instead of double precision for previous operational cycles, which doesn't impact the output of chemistry and aerosol fields.

    In the operational environment, cycle 47R1 IFS-AER assimilates AOD observations from MODIS collection 6.1 (Levy et al.,

10   2013) and from the Polar Multi Angle Product (Popp et al., 2016). The horizontal and vertical resolution as well as the time step are unchanged as compared to operational cycle 46R1, at $T_L 511$ (40 km grid cell), 137 levels over the vertical and 900s. A definition of the vertical levels can be found at https://www.ecmwf.int/en/forecasts/documentation-and-support/137-model-levels. Prognostic aerosols are used as an input of the IFS radiation scheme to compute the direct radiative effect of aerosols. Since cycle 46R1, injection heights provided by GFAS (Rémy et al. (2017)) are used for all aerosol and trace gas biomass burning

emissions. Since cycle 43R1, as detailed in Rémy et al. (2019), direct SOA emissions (scaled on anthropogenic CO emissions following Spracklen et al. (2011)) are added to organic matter emissions. A summary of the operational configurations of the latest versions of the NRT system during the CAMS and MACC projects, as well as the three reanalysis is shown in table 5.

**Table 5.** IFS-AER cycles and options used operationally for Near-Real-Time global CAMS products. MF stands for Mass fixer, DDEP for dry deposition and SCON for sulfate conversion. G01bis is for the Ginoux et al. (2001) dust emission scheme with modified distribution of the emissions into the dust bins. R05 corresponds to the version of the parameterization described in Reddy et al. (2005). R05bis is for the updated simple sulphate conversion scheme with temperature and relative humidity dependency. CF stands for the wet deposition parameterization using condensation fluxes, as implemented in cycle 46R1. L19 stands for wet deposition based on Luo et al. (2019). ZH01 and ZH14 stands for the Zhang et al. (2001) and Zhang and He (2014) dry deposition parameterizations. MACCRA, CAMSiRA and CAMSRA are the MACC Reanalysis (Inness et al. (2013)), the CAMS interim Reanalysis (Flemming et al. (2015)) and the CAMS Reanalysis (Inness et al. (2019)). For the three reanalysis, the date column refers to when the data was first publicly released.

| Model Version | Date | Resolution | Emissions | | | | MF | DDEP | WDEP | SCON |
|---|---|---|---|---|---|---|---|---|---|---|
| | | | Sea-salt | Dust | OM/BC | SO2 | | | | |
| CY37R3 | 04/2013 | T255L60 | M86 | G01 | EDGAR | EDGAR | No | R05 | R05 | R05 |
| CY40R2 | 09/2014 | T255L60 | M86 | G01 | EDGAR | EDGAR | No | R05 | R05 | R05 |
| CY41R1 | 09/2015 | T255L60 | M86 | G01 | EDGAR | EDGAR | No | R05 | R05 | R05 |
| CY41R1 | 06/2016 | T511L60 | M86 | G01 | EDGAR | EDGAR | No | R05 | R05 | R05 |
| CY43R1 | 01/2017 | T511L60 | M86 | G01bis | MACCity + SOA | MACCity | Yes | R05 | R05 | R05 |
| CY43R3 | 09/2017 | T511L60 | M86 | G01bis | MACCity + SOA | MACCity | Yes | R05 | R05 | R05bis |
| CY45R1 | 06/2018 | T511L60 | G14 | G01bis | MACCity + SOA | MACCity | Yes | ZH01 | R05 | R05bis |
| CY46R1 | 07/2019 | T511L137 | G14 | N12 | CAMS_GLOB + SOA | CAMS_GLOB | Yes | ZH01 | CF | CB05 |
| CY47R1 | 10/2020 | T511L137 | A16 | N12 | CAMS_GLOB + SOA | CAMS_GLOB | Yes | ZH01 | CF | CB05 |
| CY47R2 | 05/2021 | T511L137 | A16 | N12 | CAMS_GLOB + SOA | CAMS_GLOB | Yes | ZH01 | CF | CB05 |
| CY47R3 | 10/2021 | T511L137 | A16 | N12 | CAMS_GLOB + SOA | CAMS_GLOB | Yes | ZH14 | L19 | CB05 |
| MACCRA | 2013 | T255L60 | M86 | G01 | EDGAR | EDGAR | No | R05 | R05 | R05 |
| CAMSiRA | 2015 | T159L60 | M86 | G01 | EDGAR | EDGAR | No | R05 | R05 | R05 |
| CAMSRA | 2018 | T255L60 | M86 | G01bis | MACCity +SOA | MACCity | Yes | R05 | R05 | R05bis |

## 4 Aerosol primary sources

5   This section described the updates in the parameterizations of online aerosol emissions for dust and sea-salt aerosol since cycle 45R1.

## 4.1 Sea-salt

In addition to the Monahan86 (Monahan et al. (1986)) and the Grythe14 Grythe et al. (2014) sea-salt aerosol emission schemes, a new sea-salt emission scheme based on Albert et al. (2016) has been developed. It is similar to the Monahan86 scheme in the sense that as a prerequisite, the oceanic whitecap fraction is first estimated; in the Monahan86 scheme this is done following

5 the work ofMonahan and Muircheartaigh (1980). In the Albert16 scheme, this is done by a statistical fit between a dataset of one year of whitecap fraction estimated from remote sensing observations of ocean surface brightness by radiometers onboard the WindSat satellite, at two frequencies: 10 and 37 GHz (Anguelova and Webster (2006)), and 10m wind speed provided by Quickscat as well as sea-surface temperature provided by ERA interim. The whitecap fraction $W$ is expressed as a function of 10m windspeed $U_{10}$ and $SST$ by :

10 $$W = a(SST) \left[U_{10} + b(SST)\right]^2 \tag{1}$$

where

$$a(SST) = a_0 + a_1 SST + a_2 SST^2$$
$$b(SST) = b_0 + b_1 SST$$

The $a_{0,1,2}$ and $b_{0,1}$ parameters are given in Albert et al. (2016) for the whitecap fraction estimated with WindSat 10 and 37

15 GHz brightness temperature. In the IFS-AER implementation of this scheme, using the fit to whitecap from 37 GHz brightness temperature gave better results, and the $a_{0,1,2}$ and $b_{0,1}$ parameters for this wavelength were chosen.

Using the oceanic whitecap fraction as an input, the production flux of sea-salt aerosol is then computed by the following formula from (Monahan et al., 1986):

$$\frac{dF}{D_p} = 3.6 \, 10^5 \, W \, D_p^{-3} (1 + 0.057 D_p^{1.05}) 10^{1.19 \exp(-B^2)} \tag{2}$$

20 where

$$B = \frac{0.38 - \log(D_p)}{0.65} \tag{3}$$

and $D_p$ is the particle diameter.

Table 6 shows the simulated emissions, burden and lifetime of the three sea-salt bins for the three available emission schemes. The emissions of super coarse sea-salt aerosol are much higher with the G14 scheme as compared to the two others. Similarly

25 to the M86 scheme, the A16 scheme shows a relatively smaller increase in emissions with bin size. The lifetime of coarse and super coarse sea-salt bins is the lowest with the A16 scheme. The M86 scheme has been used operationally until cycle 43R3. The G14 scheme has been used operationally in cycles 45R1 and 46R1, while the new A16 scheme has been implemented in operational CY47R1 IFS-AER.

An evaluation of this new scheme has been carried out against collocated AOD at 550nm observations from the Maritime

30 Aerosol Network (MAN, Smirnov et al. (2009), against AOD at 550nm from a selection of 14 AERONET (Holben et al. (1998))

**Table 6.** Dry sea-salt aerosol emissions, burden and lifetime simulated by IFS-AER with the Monahan86, Grythe14 and Albert16 schemes. The emissions are in Tg.yr$^{-1}$, the burdens are in Tg and the lifetimes are in days.

| process | bin1 | bin2 | bin3 | total |
|---------|------|------|------|-------|
| Emissions (M86) | 32.2 | 2767.2 | 3363.8 | 6163.2 |
| Burden (M86) | 0.09 | 3.53 | 1.43 | 5.05 |
| Lifetime (M86) | 1.0 | 0.46 | 0.16 | 0.29 |
| Emissions (G14) | 41.6 | 1799.5 | 45531.6 | 47372.7 |
| Burden (G14) | 0.14 | 2.86 | 22.5 | 25.5 |
| Lifetime (G14) | 1.3 | 0.58 | 0.18 | 0.2 |
| Emissions (A16) | 110.3 | 6595.5 | 13657.8 | 20363.6 |
| Burden (A16) | 0.39 | 4.46 | 1.41 | 6.2 |
| Lifetime (A16) | 1.3 | 0.25 | 0.04 | 0.11 |

stations more representative of sea-salt aerosols, and against climatological monthly sea-salt aerosol surface concentration observations from the AEROCE/SEAREX programme.The AERONET stations used are: Ragged Point, Reunion St Denis, Noumea, Midway Island, Key Biscayne, Key Biscayne2, Cape San Juan, Edinburgh, Cabo da Roca, ARM Graciosa, American Samoa, Amsterdam Island, Andenes and Birkenes. Figure 3 shows the evaluation against total AOD at 550nm from the MAN

5 network. Total AOD provided by MAN cruises generally, but not always, consist mostly of sea-salt aerosol optical depth. Occasionally, dust or biomass burning plumes can also have an impact, but this impacts a minority of the measurements. Figure 3 shows that a small positive bias of 0.016 of simulated AOD at 550nm against MAN data turns into a small negative bias of -0.02, with little changes in correlation. The root mean square error (RMSE) is slightly improved with CY47R1, decreasing from 0.115 to 0.111.

10     In order to assess the skill of simulated surface concentration of sea-salt aerosol, observations of sea-salt aerosol surface concentration carried out in the AEROCE and SEAREX programmes of the 1980s and 1990s are used as monthly climatologies. These observations were carried out by the University of Miami. As detailed in Jaeglé et al. (2011), these observations were carried out in ambient conditions with PM10 inlets, which is nearly consistent with the sum of bin1 and bin2 surface concentration (ie sea-salt aerosols with a radius at 80% relative humidity of up to 5 microns). Figure 4 shows that a small negative bias

15 of 6.4 $\mu g/m^3$ with CY45R1 is significantly reduced with CY47R1, and that RMSE is also lowered. The low bias of CY45R1 may seem inconsistent with the high bias in simulated AOD against MAN observations, but this apparent inconsistency can be explained by the fact that only the sum of bin1 and bin2 is used in the comparison against AEROCE/SEAREX data, while most of the sea-salt aerosol emissions and burden in cycle 45R1 concern bin3, as shown in table 6.

    Finally, figure 5 compared simulated and observed AOD at 550nm over a selection of 14 AERONET sites that are more

20 representative of sea-salt aerosol. The same remark can be made as for the MAN observations, ie that non sea-salt aerosol probably contributes to some of the observed and simulated values, and thus reduces the significance of this evaluation. How-
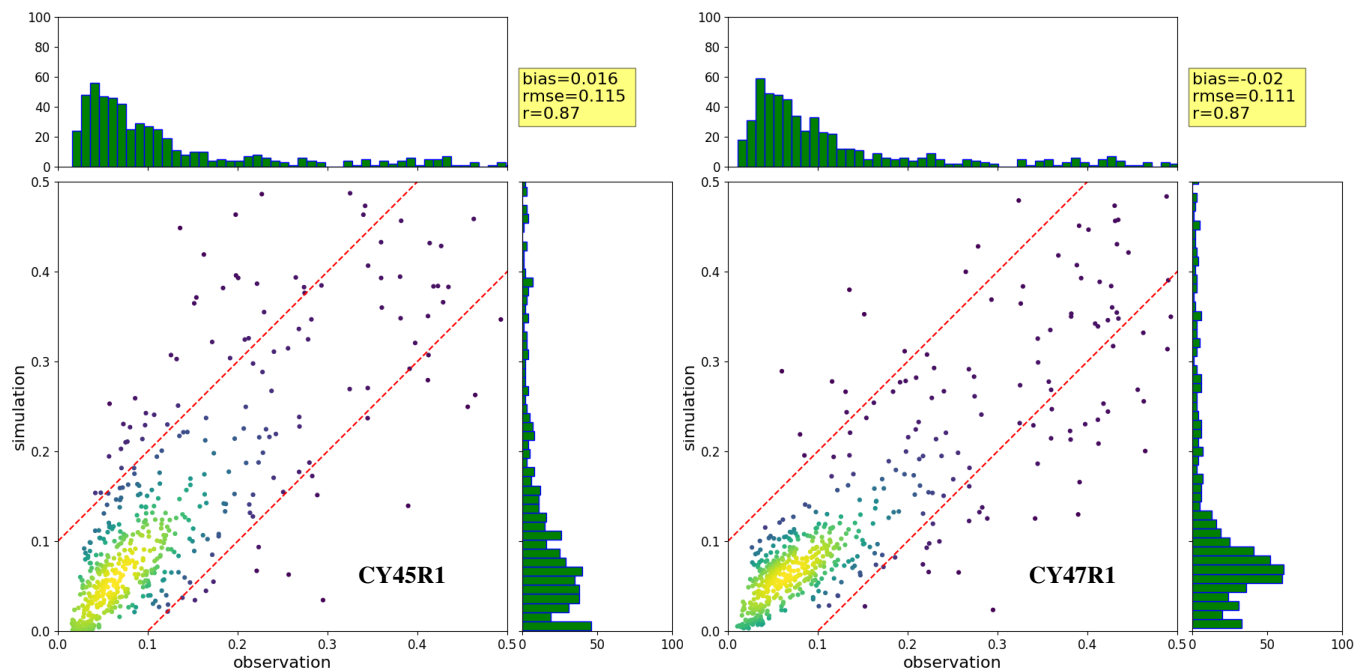
**Figure 3.** 2017: density scatterplot of AOD at 550nm simulated by IFS-AER (cycle 45R1 on the left, cycle 47R1 on the right) and observed by the MAN network.

ever, with a careful selection of AERONET sites, it is likely that the contribution of non sea-salt aerosols is much lower than that of sea-salt aerosol. The improvement with CY47R1 is very clear, with a significantly reduced bias and a much improved RMSE as compared to CY45R1, although correlation is low in both cases.

## 4.2 Desert dust

5 A new dust emission scheme has been implemented since cycle 46R1, which combines the approaches of Marticorena and Bergametti (1995) for the representation of the saltation process and of Kok (2011) for the size distribution of dust at emissions. This new dust scheme was adapted from the scheme implemented in TACTIC (Michou et al. (2015), Nabat et al. (2012)).

The emissions of dust particles of a given size $D_p$ through sandblasting occurs if the wind friction velocity $u^*$ is above a threshold value $u_t^*(D_p)$, written as:

10 $$u_t^*(D_p) = u_{ts}^*(D_p) f_{eff} f_w \tag{4}$$
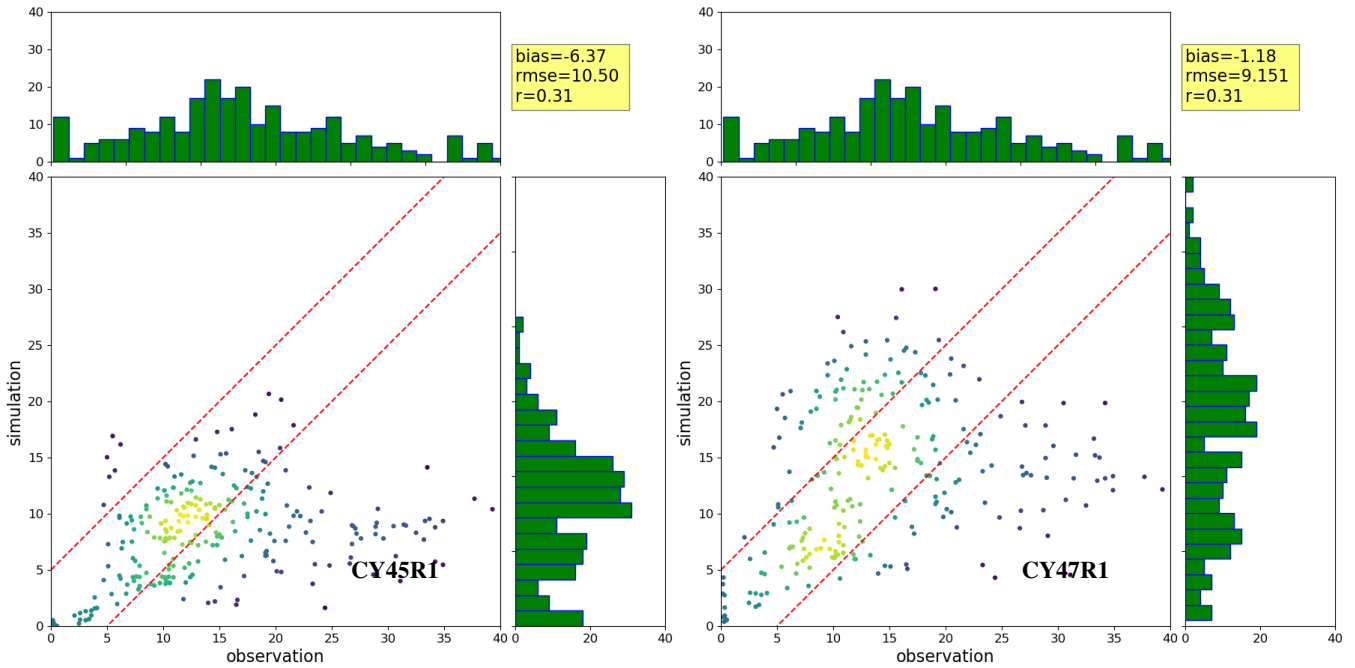
**Figure 4.** 2017: density plot of monthly simulated (CY45R1 on the left; CY47R1 on the right) sea-salt surface concentration in $\mu g/m^3$ (sum of bin1 and bin2) vs climatological values from 21 AEROCE/SEAREX stations.
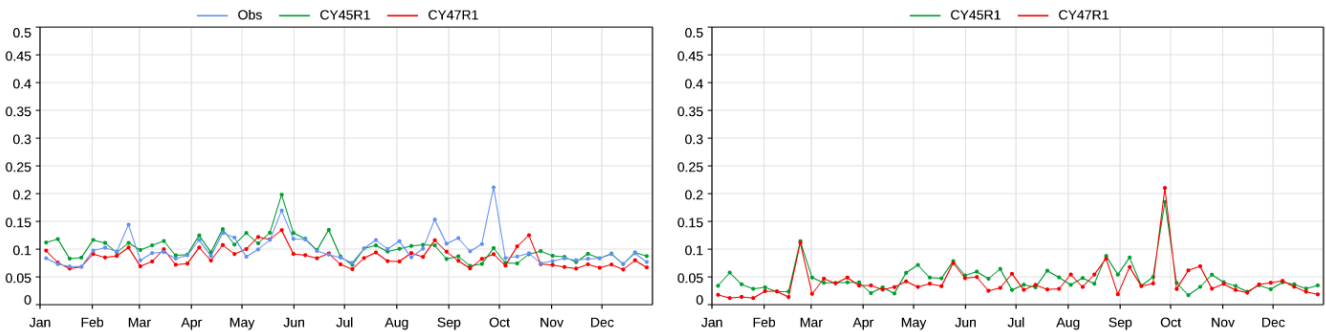
**Figure 5.** Left, observed and simulated AOD in 2017 over a selection of 14 AERONET stations more representative of sea-salt aerosol. Right, RMSE of simulated AOD against AERONET AOD at these fourteen stations.

Where $u_t^* s(D_p)$ represents an ideal minimum threshold friction velocity and is determined according to the parameterization of Marticorena and Bergametti (1995) as a function of the Reynolds number $R_e$:

$$u_{ts}^*(D_p) = \begin{cases} 0.129 \times K \times [1 - 0.858 \times exp(-0.0617(R_e - 10))] & R_e > 10 \\ \dfrac{0.129 \times K}{\left(1.928 \times R_e^{0.092} - 1\right)^{0.5}} & R_e \leq 10 \end{cases} \qquad (5)$$

Where the Reynolds number $R_e$ is parameterized following Marticorena and Bergametti (1995) as

$$R_e = 1331.647 \times D_p^{1.561228} + 0.38194 \tag{6}$$

and

$$K = \sqrt{\frac{2 \times g \times \rho_p \times D_p}{\rho_a} \times \left[1 + \frac{0.006}{\rho_g \times g \times (2 \times D_p)^{2.5}}\right]} \tag{7}$$

Where $\rho_p$ is the dust aggregate density taken as 2.6 $kg/m^3$, $\rho_a$ is the surface air density and $g$ the gravitational constant. The term $f_{eff}$ is a correction factor accounting for the effect of surface roughness, expressed as:

$$f_{eff} = 1 - \left[\frac{ln\left(\frac{z_m}{z_0}\right)}{ln\left(0.35\left(\frac{10}{z_{0s}}\right)^{0.8}\right)}\right] \tag{8}$$

Finally, $f_w$ accounts for the effect of soil moisture content on the threshold friction velocity. Following Fecan et al. (1999), it is parameterized as:

$$f_w = \begin{cases} [1 + 1.21 \times (w - w')^{0.68}]^{0.5} & \text{for } w > w' \\ 1 & \text{for } w < w' \end{cases} \tag{9}$$

Where $w$ is the surface soil moisture, provided by the IFS surface scheme, and

$$w' = 0.0014 \times (\%clay)^2 + 0.17 \times (\%clay) \tag{10}$$

Where %clay is the fraction of soil that is composed of clay. The information on the clay, silt and sand fraction is provided externally by the Global Soil Data set for use in Earth system models (GSDE, Shangguan et al. (2014). The horizontal flux of dust from saltation is expressed as:

$$G = E_{soil} \times \frac{\rho_a}{g} \times S_{rel} \times (u^*)^3 * \left(1 - \left(\frac{u_t^*}{u^*}\right)^2\right) \times \left(1 + \frac{u_t^*}{u^*}\right) \tag{11}$$

Where $E_{soil}$ is the soil "erodibility" and $S_{rel}$ is the ratio of the surface of the dust aggregate of diameter $D_p$ over the sum of the surface of aggregates of all diameters. The soil erodibility can be defined as the soil erosion efficiency of a surface under a given meteorological forcing (Zender et al. (2003)). It is also often denoted as "dust source function". Because soil erodibility is hard to estimate, several methods have been tested in dust emission schemes, one of the most commonly used is the topographic approach from Ginoux et al. (2001), which assumes that the topographic depressions are the largest source of dust. In the operational cyle 47R1, the soil erodibility is provided empirically by a climatological dataset of the frequency of occurrence of dust AOD > 0.4, as provided by Paul Ginoux and introduced in Ginoux et al. (2012). In cycle 46R1, the climatological frequency of dust AOD > 0.2 was used, which led to an overestimation of simulated dust AOD.

The friction velocity $u^*$ is computed using as an input the 10m wind speed that includes a gustiness effect, computed as in Rémy et al. (2019). Finally, the flux of vertically emitted dust is computed from the horizontal flux using Gilette (1979):

$$H = G \times F_{bare} \times C \times \begin{cases} 10^{0.134 \times (\%clay) - 6.0} & \text{for } \%clay \leq 17\% \\ 10^{-0.09 \times (\%clay) - 2.19} & \text{for } \%clay > 17\% \end{cases} \tag{12}$$

**Table 7.** Desert dust emissions, burden and lifetime simulated by IFS-AER with the Ginoux01 (G01) and Nabat12 (N12) schemes. The emissions are in $Tg.yr^{-1}$, the burdens are in $Tg$ and the lifetimes are in days.

| process | bin1 | bin2 | bin3 | total |
|---|---|---|---|---|
| Emissions (G01) | 87.9 | 292 | 2054.9 | 2434.8 |
| Burden (G01) | 1.7 | 5.9 | 8.5 | 16.1 |
| Lifetime (G01) | 7.0 | 7.2 | 1.5 | 2.4 |
| Emissions (N12) | 4.9 | 45.2 | 3248.5 | 3298 |
| Burden (N12) | 0.12 | 1.0 | 13.5 | 14.6 |
| Lifetime (N12) | 8.9 | 8.1 | 1.5 | 1.6 |

where $F_{bare}$ is the fraction of the soil that is bare; C is a normalization constant set to 0.034, nearly similar to the value used in Nabat et al. (2012) who used 0.035. This formula is integrated for all particle diameters $D_p$ and provides the total flux of emitted dust. In order to distribute this flux into the three bins, the size distribution at emissions of Kok (2011) is used, which means a much larger share of emissions being distributed to the super coarse bin as compared to the Ginoux et al. (2001) scheme used operationally before cycle 46R1. This is illustrated by Table 7, and as a consequence the simulated lifetime of total dust is significantly lower with the new scheme as compared to the old scheme, because the super coarse dust bin has a much shorter lifetime from increased dry deposition and sedimentation.

The sum of all dust emissions with the two emission schemes is shown in Figure 6. There is a much higher regional variability of yearly averaged dust emissions with the new scheme. Also, dust emissions are higher in the Sahel and many parts of the Sahara, and mostly lower over the Taklamakan and Gobi deserts. In order to evaluate and compare the skills of the two schemes, the simulated AOD at 500nm has been compared against values observed at a selection of AERONET stations that are dominated by dust. Figure 7 shows such a comparison: despite higher emissions, the simulated dust AOD is significantly lower in average of the selected stations. A positive bias with the older scheme turns into a small negative bias. The skill of the simulated dust seems to improve with the new scheme, as RMSE is generally decreased and sometimes halved. The spatial correlation is also generally improved.

In order to focus specifically on simulated dust AOD, the simulated dust AOD by IFS-AER CY45R1 and CY47R1 has been compared against daily dust AOD at 550nm provided by the ModIs Dust AeroSol (MIDAS, Gkikas et al. (2020)) dataset. This novel dataset provides high resolution daily dust AOD at 550nm for the 2003-2017 period, by merging information from MODIS and MERRA-2. Figure 8 shows the retrieved dust AOD at 550nm averaged over 2017, as well as the collocated average as simulated by IFS-AER CY45R1 and CY47R1. The simulated dust AOD exhibits strong overestimation over the Taklamakan/Gobi region with IFS-AER, as well as a less pronounced overestimation over most of the other dust producign regions. With IFS-AER, the simulated values are generally closer, as shown by the reduced averaged RMSE. Over a few areas, such as the south of the Arabic Peninsula, and over the Atlantic, the RMSE is larger with CY47R1.
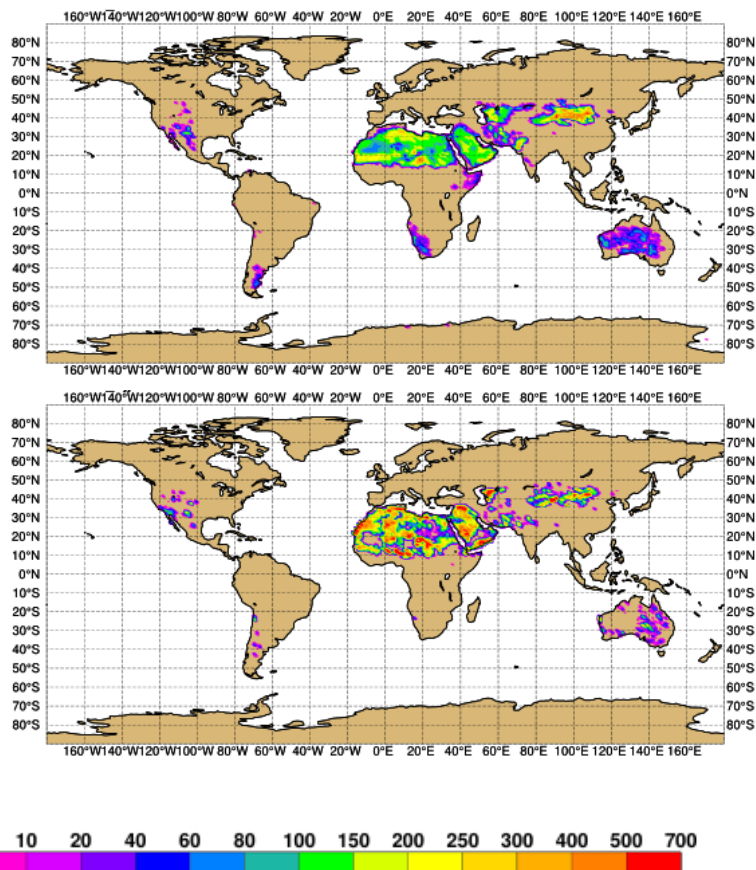
**Figure 6.** 2017 total emissions of dust as simulated by IFS-AER CY45R1 and CY47R1 (bottom), in $g\,m^{-2}\,yr^{-1}$.

## 5   Removal processes

In this section, updates to the removal processes as compared to the parameterizations implemented in cycle 45R1 of IFS-AER and described in Rémy et al. (2019) are presented.

### 5.1   Dry deposition

5   A new parameterization of aerosol dry deposition following Zhang and He (2014) has been implemented in cycle 47R1 IFS-AER, but is not used operationally for technical reasons, and is expected to be used in CY47R3. The operational dry deposition scheme still follows the approach of Zhang et al. (2001), as adapted in Rémy et al. (2019). The Zhang and He (2014) has been implemented because it gave good results in a recent intercomparison of dry depostion schemes (Khan and Perlinger (2017)), and also because instead of use the particle size as an input, it divides particles in size ranges: fine, coarse and giant

10   (super-coarse). Only the surface resistance differs as compared to the Zhang et al. (2001) scheme. The inverse of the surface
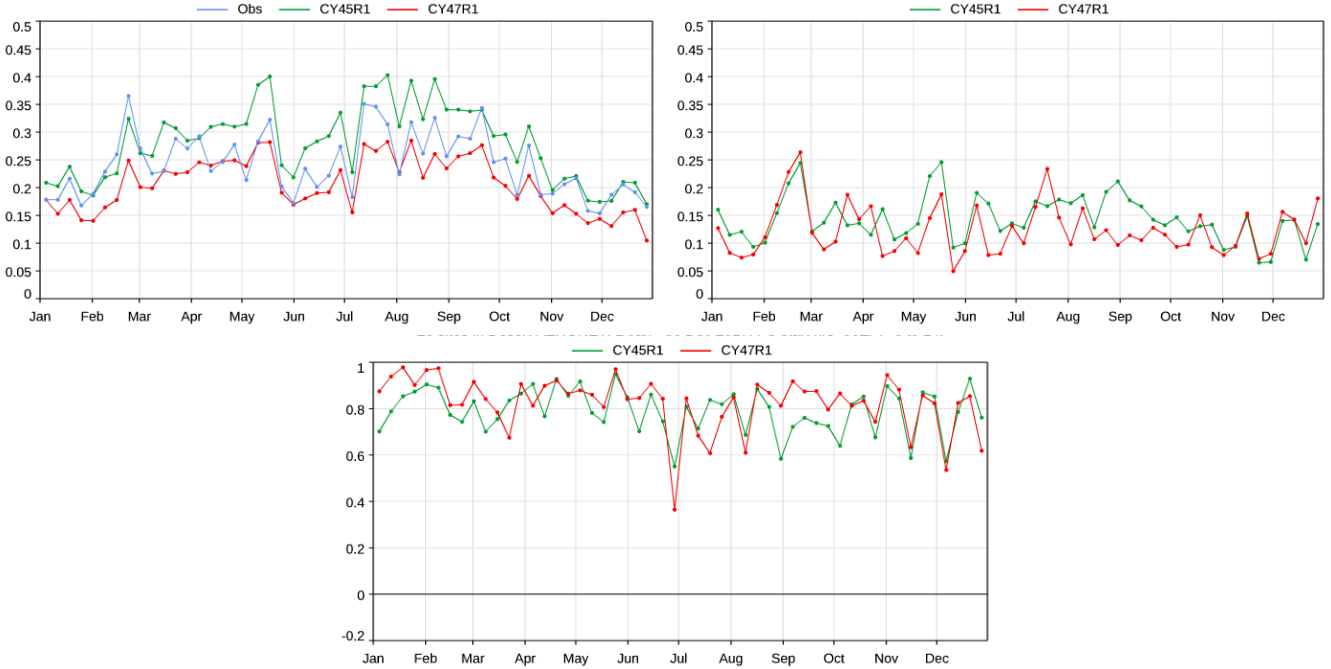
**Figure 7.** Left, observed and simulated AOD in 2017 over a selection of 24 AERONET stations more representative of desert conditions. Right, RMSE of simulated AOD against AERONET AOD at these 24 stations. Bottom, spatial correlation between simulated and observed AOD at 500nm. The AERONET stations used in this plot are: Tizi Ouzou, Tamanrasset INM, Sede Boker, Mezaira, Masdar Institute, Lampedusa, KAUST Campus,Izana, Tunis Carthage, Ilorin, Santa Cruz Tenerife, La Laguna, Dakar, Dalanzadgad, Cairo EMA, Dushanbe, Arica, Gobabeb, Windpoort, Ben Salem, Capo Verde, La Parguera, Teide, El$_F$ arafra

resistance is also referred to as surface deposition velocity and denoted as $V_s$. It is computed as as a function of the particle diameter $D_p$ and friction velocity $u^*$ as :

$$V_s = \begin{cases} a_1 \times u^* & \text{for } D_p \leq 2.5 \mu m \\ (b_1 \times u^* + b_2 \times u^{*2} + b_3 \times u^{*3}) \times exp(K_1 \times (\frac{LAI}{LAI_{MAX}} - 1)) & \text{for } 2.5 \mu m < D_p \leq 10 \mu m \\ (d_1 \times u^* + d_2 \times u^{*2} + d_3 \times u^{*3}) \times exp(K_2 \times (\frac{LAI}{LAI_{MAX}} - 1)) & \text{for } D_p > 10 \mu m \end{cases} \tag{13}$$

Where

$$K_1 = \qquad\qquad c_1 \times u^* + c_2 \times u^{*2} + c_3 \times u^{*3}$$

$$K_2 = \qquad\qquad e_1 \times u^* + e_2 \times u^{*2} + e_3 \times u^{*3} \times SST$$
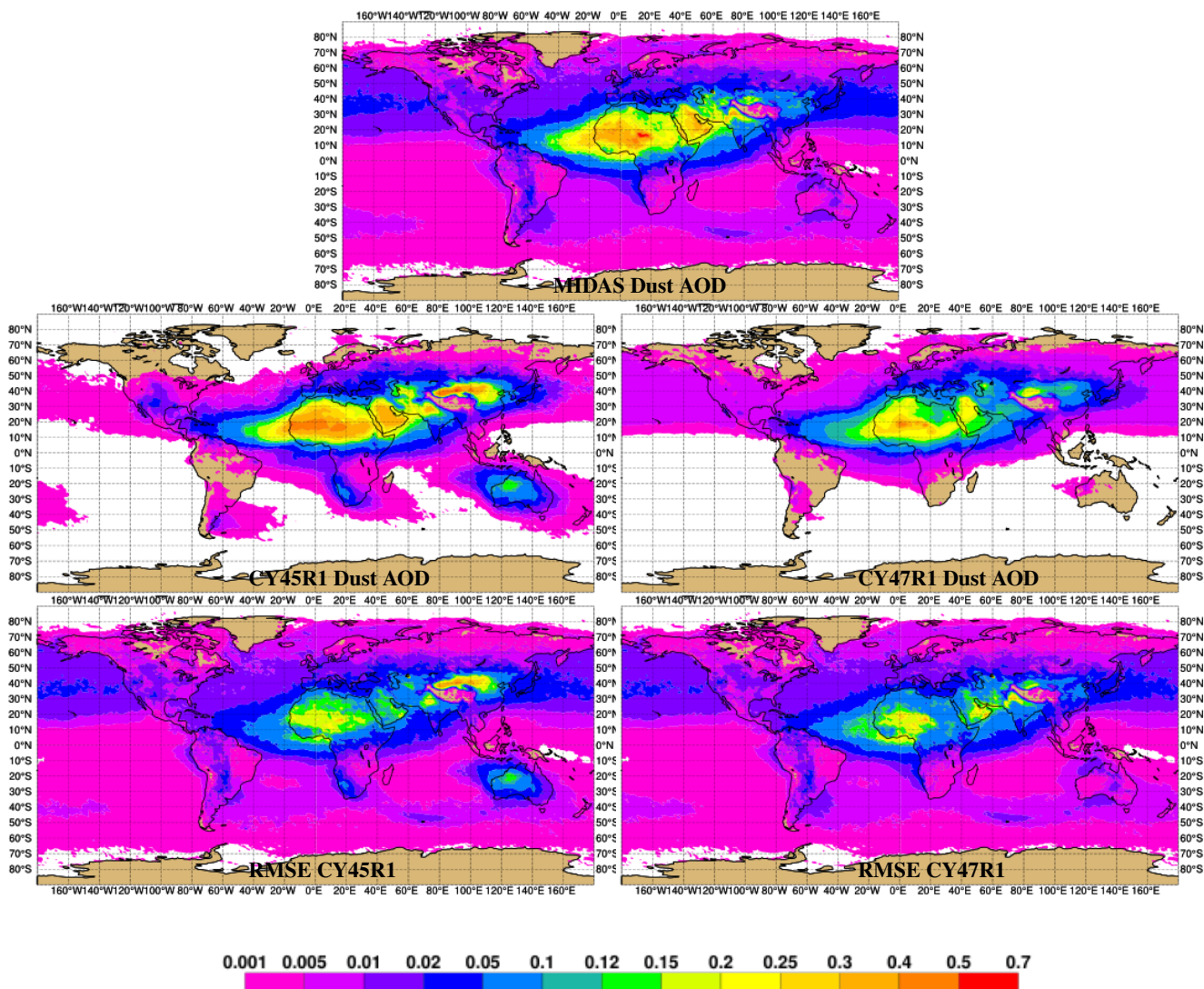
**Figure 8.** Top: 2017 average of MIDAS dust AOD at 550nm. Middle, collocated 2017 average of dust AOD at 550nm simulated by IFS-AER CY45R1 (left) and CY47R1 (right). Bottom, 2017 average of daily RMSE of simulated dust AOD at 550nm; CY45R1 (left) and CY47R1 (right).

Where $a_i, b_i, c_i, d_i, e_i$ are land-surface dependent coefficients are provided by Zhang and He (2014). $LAI_{MAX}$ is the maximum leaf area index for a give land surface category. Figure 9 shows a comparison of the simulated dry deposition velocity by the two schemes over a particular land surface category (desert).
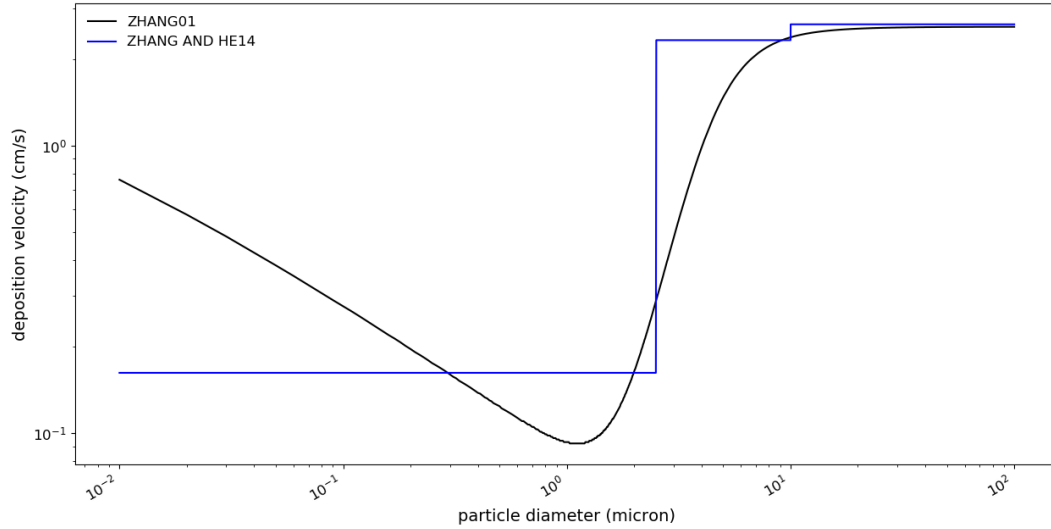
**Figure 9.** Dry deposition velocity over a desertic surface as a function of particle size, parameterized by the Zhang et al. (2001) and the Zhang and He (2014) schemes.

## 5.2 Wet deposition

### 5.2.1 In-cloud scavenging in cycle 46R1

Several updates have been brought to the representation of in-cloud scavenging in cycle 46R1. The in-cloud scavenging rate in s$^{-1}$ at model level $k$ of an aerosol $i$ is written as follows:

$$W^{I}_{i,k} = exp(-\beta_k * D_i) \times f_k \qquad (14)$$

where $D_i$ is the fraction of aerosol $i$ that is included in water and ice droplets and $f_k$ is the cloud fraction at level $k$. The value of the parameter $D_i$ is different for water and ice droplets; for water droplets, the values of $D_{iw}$ from Table 8 are used. Following Bourgeois and Bey (2011), for ice droplets, $D_{ic}$ is set to 0.06 for all aerosols. The final value of $D_i$ is computed from $D_{iw}$ and $D_{ic}$ by weighting with the ice and water cloud droplet mass mixing ratio $m_c$ and $m_w$ respectively:

$$D_i = \frac{m_w \times D_{iw} + m_c \times D_{ic}}{m_w + m_c} \qquad (15)$$

$\beta_k$ is the rate of conversion of cloud water to rain water. Before cycle 46R1, as described in Rémy et al. (2019), $\beta_k$ was computed following Giorgi and Chameides (1986), $\beta_k$, by comparing the precipitation flux at levels $k$ and $k+1$. In cycle 46R1, a new approach has been tested, using the cloud ice and water condensation fluxes instead:

$$\beta_k = (C_{w,k} + C_{c,k}) \times (\rho_k \, \Delta z_k \, f_k \, q_k) \qquad (16)$$

**Table 8.** Value of the parameter $D_w$, representing the fraction of aerosol included in water cloud droplet.

| Species $i$ | $D_iw$ value |
|---|---|
| Sea-salt | 0.9 |
| Dust | 0.7 |
| OM hydrophilic | 0.7 |
| BC hydrophilic | 0.7 |
| Sulfate | 0.7 |
| Nitrate | 0.8 |
| Ammonium | 0.9 |

Where $C_{w,k}$ and $C_{c,k}$ are the cloud ice and water condensation fluxes at level $k$, $q_k$ the sum of the liquid and ice mass mixing ratio and $\Delta z_k$ is the layer thickness of the model level $k$

The representation of the re-evaporation process has also been complexified. The release of aerosol particles contained in rain drops at level $k$ occurs if evaporation of precipitation is diagnosed, i.e. if the precipitation flux at level $k$ is higher than at level $k+1$, where level $k+1$ is below level $k$. If there is no precipitation at level $k+1$, then all aerosols that have been subjected to in-cloud scavenging at or above level $k$ are released. If the precipitation flux at level $k+1$ is not null, then the re-evaporation is partial. Before cycle 46R1, it was assumed arbitrarily that half of the scavenged aerosols at or above level $k$ are then released. Since cycle 46R1, a more complex parameterization has been implemented, following de Bruine et al. (2018). The mass of an aerosol species $i$ that is re-evaporated at level $k$ is computed as a function of the fraction of evaporated precipitation defined with the precipitation flux at level k $P_k$, $\epsilon_k = \frac{P_{k+1} - P_k}{P_k}$:

$$\delta M_{i,k}^{evap} = \epsilon_k \times \left( \left[ 1 - exp^{-2\sqrt{\epsilon_k}} \left( 1 + 2 \times \epsilon_k^{\frac{1}{2}} + 2 \times \epsilon_k + \frac{4}{3} \epsilon_k^{\frac{3}{2}} \right) \right] \times (1 - \epsilon_k) + \epsilon_k^2 \right) \times Loss_{scav,i,k} \tag{17}$$

Where $Loss_{scav,i,k}$ is the sum of the mass of aerosol that is subjected to in-cloud wet deposition from level $k$ to the model top.

### 5.2.2 In-cloud scavenging in cycle 47R1

In cycle 47R1 a new optional formulation of the in-cloud scavenging rate has been implemented, **which is not yet used operationally for technical reasons, but should be used in operational cycle 47R3**. This formulation follows the approach of Luo et al. (2019). For liquid precipitation,

$$W_{i,k}^{\mathrm{I}} = exp\left( -D_{i,w} \times \left[ K_{min} + \frac{\beta_{k,r}}{q_{k,r,tot}} \right] \right) \times \frac{f_k \times \beta_{k,r} \times q_{k,r,tot}}{\left( K_{min} + \frac{\beta_{k,r}}{q_{k,r,tot}} \right)} \tag{18}$$

Where $q_{r,k,tot}$ is derived from the liquid water mass mixing ratio $q_k$ by $q_{k,r,tot} = q_k + \delta_t \times \beta r, k$, where $\delta t$ is the time step. $K_{min}$ is the minimum value of rainout loss rate, set to $0.0001 s^{-1}$ in Luo et al. (2019). $D_{i,w}$ is provided by table 8, and $\beta_{r,k}$ is defined

**Table 9.** Value of the parameters $\alpha_r$ and $\alpha_i$.

| Species | $\alpha_r$ | $\alpha_i$ |
|---|---|---|
| Seasalt fine | 0.001 | 0.005 |
| Seasalt coarse | 0.001 | 0.005 |
| Seasalt super coarse | 0.1 | 0.005 |
| Dust fine | 0.001 | 0.005 |
| Dust coarse | 0.001 | 0.005 |
| Dust super coarse | 0.1 | 0.005 |
| OM hydrophilic | 0.0001 | 0.005 |
| OM hydrophobic | 0.0001 | 0.005 |
| BC hydrophilic | 0.0001 | 0.005 |
| BC hydrophobic | 0.0001 | 0.005 |
| Sulphate | 0.0001 | 0.005 |
| Nitrate fine | 0.0001 | 0.005 |
| Nitrate coarse | 0.1 | 0.005 |
| Ammonium | 0.0001 | 0.005 |

as in Giorgi and Chameides (1986) using the rain flux at level k $P_{r,k}$:

$$\beta_{r,k} = (P_{r,k+1} - P_{r,k}) \times (\rho_k \, \Delta z_k) \tag{19}$$

The formulation of Luo et al. (2019) applies only to liquid precipitations. It has been extended for solid precipitations, but taking into account the smaller fraction of aerosols included in solid precipitations, the value the $D_i$ parameter is divided by
5 two for solid precipitations. The scavenging rates for solid and liquid precipitations are then added.

### 5.2.3 Below-cloud scavenging in cycle 46R1 and 47R1

Since cycle 46R1, the below cloud scavenging rate is expressed by:

$$W_{i,k}^{\text{B}} = fp_k \times \left[ (1 - exp(P_{r,k} \times \alpha_r)) + (1 - exp(P_{i,k} \times \alpha_i)) \right] \tag{20}$$

Where $P_{r,k}$ and $P_{i,k}$ are the fluxes of liquid and solid precipitation respectively, $fp_k$ is the fraction of grid cell at level $k$
10 in which precipitation occurs, and $\alpha_r$ and $\alpha_i$ the efficiency with which aerosol variables are washed out by rain and snow, respectively. The values used have been derived from Croft et al. (2009) and are summarized in table 9.

### 5.2.4 Evaluation of wet deposition fluxes against CASTNET data

The simulated sulfur wet deposition fluxes for 2017 are shown in Figure 10. Besides wet deposition, other model changes impacted wet deposition fluxes between cycle 45R1 and 47R1, in particular the changes in sulfate production. This sulphur
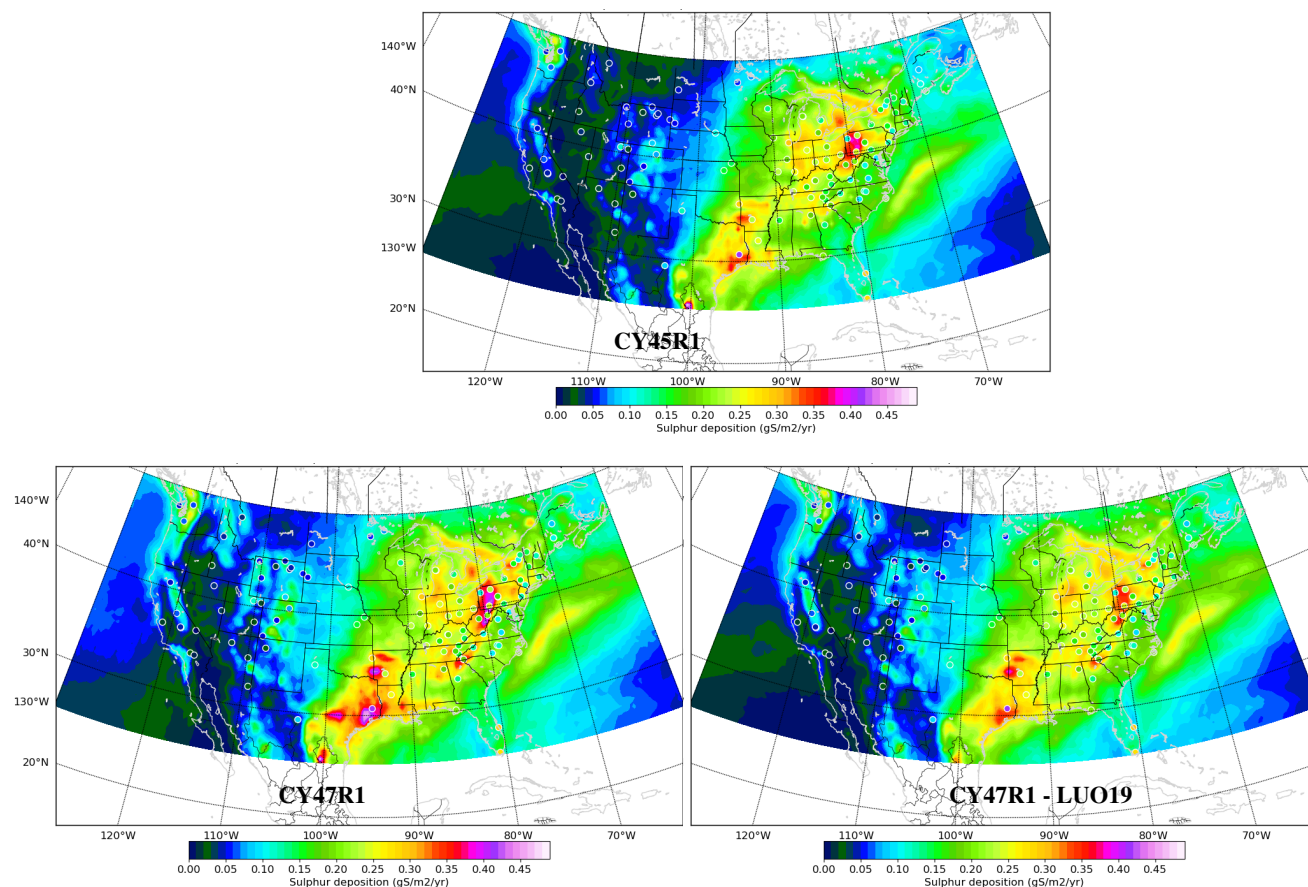
**Figure 10.** 2017 simulated vs retrieved wet deposition flux of sulphur over the United States.

wet deposition fluxes increased with CY47R1, but this can be caused by changes in wet deposition and/or because of a higher sulfate conversion rate. The simulated fluxes are slightly higher as compared to values provided by the CASTNET network. The simulated wet deposition derived from the Luo et al. (2019) approach gives slightly lower values as compared to the operational wet deposition scheme of CY47R1, which brings the simulated values closer to the observations. Overall, the agreement between the simulated and observed sulphur cycle is good for cycle 47R1 with the wet deposition adapted from Luo et al. (2019), although values can be overestimated over some mountainous areas such as the Western and Eastern fringes of the Rockies.

Table 10 presents the aggregated skill scores of the simulated yearly sulphur wet deposition fluxes over the U.S. against CASTNET data. The bias and correlation are degraded by CY47R1 as compared to CY45R1; however this is possibly a case of compensating biases, as the surface concentration of sulfate is simulated much better by CY47R1 as compared to CY45R1. The new wet deposition option improves significantly on CY47R1, but doesn't reach the values attained for CY45R1.

**Table 10.** Bias, RMSE and spatial correlation factor (R) of simulated yearly sulphur wet deposition fluxes vs CASTNET observations, in gS/m2/year.

| Experiment | bias | RMSE | Correlation |
|---|---|---|---|
| CY45R1 | 0.027 | 0.065 | 0.78 |
| CY47R1 | 0.056 | 0.085 | 0.75 |
| $CY47R1_N EW DEP$ | 0.046 | 0.075 | 0.75 |

### 5.3 Sedimentation

The computation of sedimentation fluxes is unchanged as compared to Rémy et al. (2019) and Morcrette et al. (2009). However, since cycle 47R1, it is applied to coarse sea-salt aerosol in addition to the super-coarse sea-salt and dust aerosols. Moreover, the sedimentation velocity is computed dynamically using Stokes's law as a function of particle size and density, which themselves vary as a function of relative humidity for sea-salt aerosol:

$$V_s = \frac{2\rho_{p,RH} \times g}{9\mu} r^2_{p,RH} \times C_F \tag{21}$$

where $\rho_{p,RH}$ and $r_{p,RH}$ are the particle density and radius respectively, that depends on relative humidity, $g$ the gravitational constant, $\mu$ the air viscosity and $C_F$ the Cunningham correction factor.

## 6 Budgets and simulated fields

### 6.1 Configuration of the forecast-only simulations

IFS-AER was run in cycling forecast mode, without data assimilation from January to December 2017 at a resolution of $T_L511L137$, using emissions and model options similar to the operational NRT run. Simulations has been carried out for cycle 45R1, without the coupling to the chemistry, and for cycle 47R1 with the operational set of deposition options (denoted "CY47R1") and with the wet deposition adapted from Luo et al. (2019) and dry deposition from Zhang and He (2014) (denoted "CY47R1_NEWDEP"). Budgets are shown for February to December 2017 to allow for a month of spin-up time. The simulated AOD and PM are shown for the same period of time.

### 6.2 Budgets

Budgets are presented in Table 11 for the two cycle 47R1 experiments. For both sea-salt and dust, the particle size has an important impact on lifetime: the larger particles have a much shorter lifetime because of more active dry deposition and sedimentation. As compared to results from cycle 45R1 presented in Rémy et al. (2019), the lifetime of fine and coarse dust aerosols are noticeably longer, probably because of changes in wet deposition, which is dominant for these two bins.

Similarly, the lifetime of the other fine species: OM, BC, sulfate are significantly longer than as simulated with CY45R1; as wet deposition is the dominant sink for these species, these changes are mainly caused by the updates in wet deposition. For the biomass burning contribution of BC and OM, the use of injection heights for emissions could also contribute: when emitted at surface, biomass-burning OM and BC is immediately subjected to dry deposition, which is not the case as when emitted aloft.

5     The values indicated in Table 11 can be compared against the values from the AeroCom Phase III experiments, as reported in Gliß et al. (2021), which also includes data from IFS-AER cycle 46R1. For sea-salt aerosols, the emissions for the three bins stands at 21147 Tg/Yr, which is much higher than the aerocom median (4980 Tg/Yr) and is the highest of all models reports in Gliß et al. (2021), except for IFS-AER cycle 46R1 at more than 50000 Tg/Yr, which was using the Grythe et al. (2014) sea-salt aerosol emission scheme. This value is heavily influenced by the cutoff radius for sea-salt aerosol, which, at 20 at 80% RH, is

10    probably one of the highest. The lifetime of sea-salt aerosol is also the lowest of all models, for similar reasons: the very short lifetime of super coarse sea-salt is dominant as compared to other bins. Nevertheless, the fact that the lifetime of simulated sea-salt aerosol is significantly lower than all other models is maybe the sign that sinks are too active in the IFS. The fact that sea-salt aerosol lifetime is increased with the new deposition options goes in the right direction.

    For dust, the total emissions are simulated to reach 3297.6 Tg/Yr with IFS-CY47R1, lower than the 5650 Tg/Yr reported in

15    Gliß et al. (2021) with IFS-AER cycle 46R1. This lower value is caused by the update of the dust source function that occured in cycle 47R1, as mentioned above. The cyle 47R1 emissions are significantly higher than the Aerocom phase III median (1440 Tg/Yr) and is above all other models, as for sea-salt aerosols. Similarly to sea-salt aerosol, this can be because the cutoff radius (20 dry radius) is higher than most models. The lifetime of simulated dust stands at 1.5 days with cycle 47R1, which is much lower than the Aerocom phase III median. The most likely explanation is that the bulk of simulated dust with IFS-AER is super

20    coarse dust, both because of the high cutoff diameter and because the size distribution of emitted dust follows Kok (2011), with relatively more emissions of super coarse dust as compared to other size distributions of dust at emissions commonly used.

    Organic matter emissions, at 192 Tg/Yr are also among the highest reported in Gliß et al. (2021). This probably comes from the SOA components, as relatively few models directly emit SOA as a fraction of organic matter. The lifetime is simulated to be 4.6 days, shorter than the AeroCom phase III median (6 days), but within bounds as 4 models (out of 13, excluding

25    IFS-AER cycle 46R1) simulate shorter lifetimes for organic matter. For black carbon, there is a higher level of consensus for the emissions, which are very close between all models. The simulated lifetime, at 4.4 days, is slightly lower than the AeroCom median (5.5 days). For both organic matter and black carbon, the new deposition options bring an increase in simulated lifetime, which reduce the difference to the AeroCom median.

    Chemical production of sulfate, at 124 Tg/Yr, is quite close to the AeroCom median (143 Tg). The simulated lifetime (3.2

30    days) is shorter than the AeroCom median (4.9 days). For nitrate production, at 103.9 Tg/Yr, IFS-AER cycle 47R1 is among the highest, and much higher than the AeroCom median value of 32.5 Tg/Yr. However, the variability between AeroCom models is very high, which is partly explained by the fact that some include nitrate production from heterogeneous reactions on dust and/or on sea-salt aerosol particles (IFS-AER represents both sources). As for most of species, the simulated lifetime of nitrate, at 3 days, is shorter than the AeroCom median (3.9 days), but the variability is also high for this parameter.

**Table 11.** CY47R1 IFS-AER budgets of dry aerosols for the January to December 2017 period. Fluxes are expressed in Tg yr$^{-1}$, burdens in Tg, and lifetimes in days. Values from the CY47R1_NEWDEP experiments are shown in parentheses.

| Species | Source | Dry dep + sedim | Wet dep | Chemical conv | Burden | Lifetime |
|---|---|---|---|---|---|---|
| fine mode sea-salt | 114.2 | 9.5 (24.9) | 104.6 (89.3) | 0 | 0.3 (0.4) | 1 (1.3) |
| coarse mode sea-salt | 6850 | 5522 (5797) | 1328 (1052) | 0 | 4.5 (5.3) | 0.24 (0.27) |
| super-coarse sea-salt | 14183 | 13691 (13768) | 492 (415) | 0 | 6.1.4 (1.4) | 0.04 (0.04) |
| fine mode dust | 4.8 | 1.3 (1.6) | 3.5 (3.2) | 0 | 0.12 (0.13) | 9.1 (9.9) |
| coarse mode dust | 44.8 | 9.9 (13.8) | 34.9 (31) | 0 | 1. (1.) | 8.1 (8.1) |
| super-coarse mode dust | 3248 | 2806 (2814) | 442 (434) | 0 | 13.5 (14.4) | 1.5 (1.6) |
| Hydrophobic OM | 95.9 | 6.5 (11.2) | 8.4 (0.4) | -81 (-84.3) | 0.4 (0.4) | 1.5 |
| Hydrophilic OM | 95.9 | 17.4 (33.1) | 159.5 (147.1) | 81 (84.3) | 2.5 (2.4) | 5.1 (4.9) |
| Hydrophobic BC | 8.4 | 0.83 (1.01) | 0.57 (0.1) | -7 (-7.3) | 0.031 (0.032) | 1.3 |
| Hydrophilic BC | 2.1 | 1(1.5) | 8.5 (7.9) | 7 (7.3) | 0.13 (0.15) | 5.2 (5.8) |
| Sulfate | 0 | 5.7 (14.9) | 118.7 (109.5) | 124.4 (124.4) | 1.1 (1.2) | 3.2 (3.5) |
| Nitrate from gas-particle partitioning | 0 | 4.6 (7.6) | 35.9 (27.3) | 40.5 (34.9) | 0.47 (0.44) | 4.2 (4.6) |
| Nitrate from heterogeneous reactions | 0 | 23.8 (19.9) | 39.6 (47.7) | 63.4 (67.6) | 0.35 (0.48) | 2.1 (2.6) |
| Ammonium | 0 | 1.4 (2.4) | 17.5 (15.2) | 18.9 (17.6) | 0.15 (0.14) | 2.9 (2.9) |

## 6.3 Simulated AOD and PM

### 6.3.1 PM2.5 and PM10

Figure 11 shows the global PM2.5 and PM10 simulated by the CY47R1_NEWDEP experiment for 2017. It can be compared to Figure 11 of Rémy et al. (2019). For PM2.5, maximum values of up to 60-70 µg/m$^3$ are simulated over parts of China and

5    India, mostly from anthropogenic aerosols, and over parts of the Sahara, mostly from desert dust. Over oceans, the mean values vary between 8 and and 20 µg/m$^3$. Over Europe and Eastern U.S., the simulated values vary between 6 and 12 µg/m$^3$. Areas of seasonal biomass burning such as equatorial Africa, parts of Brazil and Indonesia show simulated PM2.5 comprised between 10 and 20 µg/m$^3$ on a yearly average. Individual large fire events, such as the "British Columbia" fire of August 2017 also appear over Western Canada, lifting the yearly average there to 10-15 µg/m$^3$.

10    Dust and sea-salt aerosols are much more prominent in the PM10 panel of Figure 11. Over oceans, the simulated PM10 varies between 20 and 35 µg/m$^3$, while yearly values can reach up to 200-300 µg/m$^3$ over the dust producing regions of the Sahara, Arabic peninsula and Taklimakan deserts. PM10 over the heavily polluted areas of India and China reach 80-100 µg/m$^3$, which is only 20-30 µg/m$^3$ more than PM2.5 over these regions, which are impacted mainly by fine particles. Similarly,
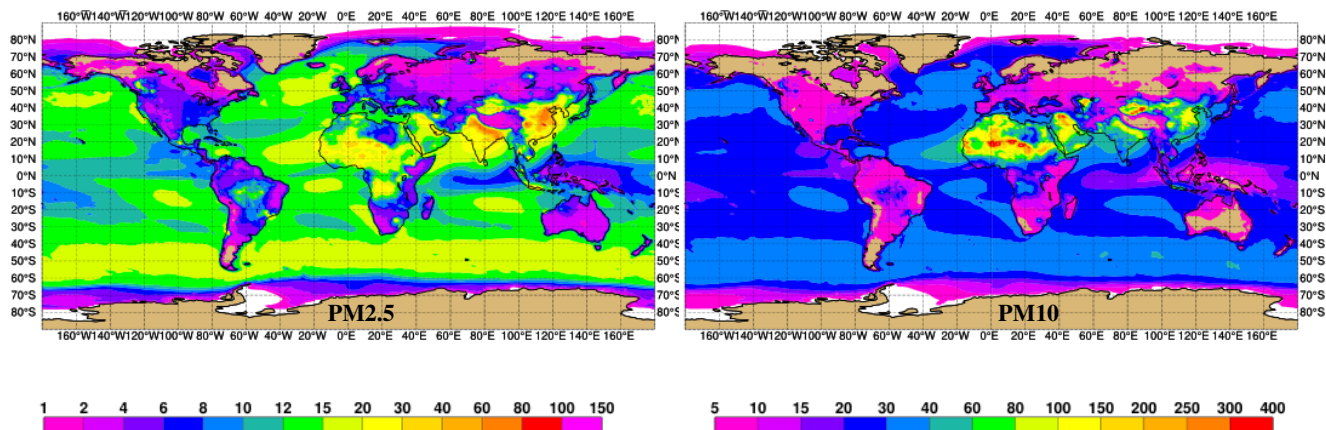
**Figure 11.** Global February-December 2017 PM2.5 (left) and PM10 (right) in µg/m³ simulated by the CY47R1_NEWDEP experiment in cycling forecast mode. Please note the different scale for PM2.5 and PM10.

the simulated PM10 values over Europe, U.S. and the seasonal biomass burning regions are 20-30% higher than the PM2.5 values.

### 6.3.2 AOD at 550nm

Figure 12 shows total and speciated AOD at 550 nm simulated by the CY47R1_NEWDEP experiment for February-December
5  2017. The highest values can be found in the heavily populated regions of the Indian subcontinent and eastern China, the dust producing regions of the Sahara, Arabic and Taklimakan deserts a, and in the seasonal biomass burning region of equatorial Africa. The transport of dust produced in the western Sahara and over the Taklimakan-Gobi deserts over the Atlantic and Pacific respectively are prominent features, which can be used to assess the deposition processes. Sea-salt AOD is quite evenly spread between the mid-latitude regions where mean winds are high, and the tropics where trade winds are on average less
10  intense, but with a relatively more active sea-salt production thanks to the dependency of sea-salt production on SST. OM is a species that combines anthropogenic and biomass burning sources: AOD are highest over parts of China and India, mostly from the source of secondary organics scaled on anthropogenic CO emissions, and equatorial Africa, from biomass burning. BC sources are also a combination of anthropogenic and biomass burning origin, the patterns are close to what is simulated for OM. Sulfate AOD is concentrated over heavily populated areas, and a few outgassing volcanoes such as Popocatepetl in
15  Mexico and Kilauea in Hawaii. Oceanic DMS sources bring a "background" of sulfate AOD over most oceans. Nitrate AOD is highest over the regions where anthropogenic emissions of nitrogen oxides are highest, over India and China. Some secondary maxima also appear over seasonal biomass burning regions, from biomass burning emissions of nitrogen oxides. Finally, the features of ammonium AOD are close to those of nitrate AOD, with lower values.

## 7  Evaluation

20  In this section, the 24h cycling forecast experiments CY45R1, CY47R1 and CY47R1_NEWDEP are evaluated against a broad range of ground and remote sensing observational datasets. The simulated AOD at 500nm is compared against level 2 ob-
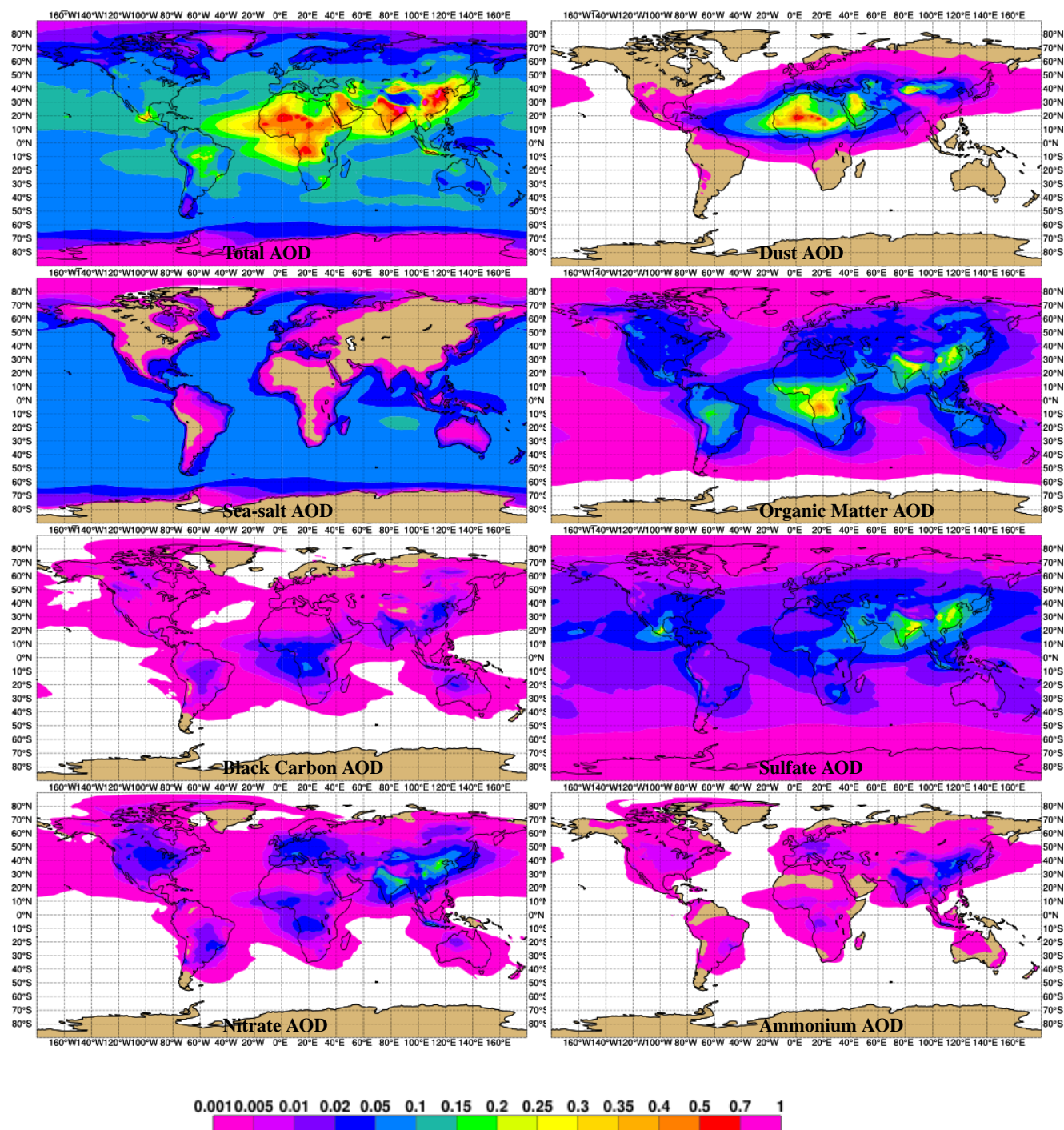
**Figure 12.** From left to right and top to bottom: February-December 2017 total, dust, sea-salt, OM, BC, sulfate, nitrate and ammonium AOD at 550 nm, simulated by the CY471_NEWDEP experiment.

servations from the Aerosol Robotic Network (AERONET; Holben et al., 1998) as well as against the merged product from Sogacheva et al. (2020). The simulated dust deposition over the Atlantic has been compared against climatological values derived from remote sensing AOD products as detailed in Yu et al. (2019). The simulated PM2.5 had been compared against observations in Europe, North America and China. Finally, the simulated surface concentration of OM has been compared

5 against observations from the IMPROVE network over the U.S., and surface concentration of nitrate and ammonium from the two CY47R1 experiments have been compared against observations from the CASTNET network over the U.S. and from the EMEP network over Europe. Some evaluation has already been shown in the preceding sections, such as dust AOD against AERONET and against the MIDAS (Gkikas et al. (2020) dataset, sea-salt AOD and surface concentration as well as sulfate surface concentration against CASTNET and EMEP measurements, and wet deposition flux against CASTNET data.

10 **7.1  Evaluation against AERONET**

Figures 13 and 14 show two measures of skill of the simulated weekly AOD at 500nm against global and regional AERONET observations. There is generally a global low bias of simulated AOD against AERONET values, of the order of 0.02-0.03 with CY45R1. This low bias is slightly worsened by CY47R1, and slightly improved by CY47R1_NEWDEP. The RMSE is generally improved by the two CY47R1 experiments, except at times in July and August 2017, when spikes in simulated AOD from

15 large fire events in the U.S. and Canada, and associated error occur with 47R1, but are much reduced with CY47R1_NEWDEP. The regional skill scores against AERONET are more varied. Over Europe, the low bias with CY45R1 is significantly improved with the two CY47R1 experiments, and associated with a reduced RMSE. Several factors can explain this improvement; the dominant cause is probably the presence of nitrate/ammonium aerosols in the CY47R1 experiments. Over North America, the simulated low bias with CY45R1 turns to a small positive bias with 47R1, and at times very large during fire events in

20 July/August and December. The positive bias of CY47R1 is much improved with CY47R1_NEWDEP, for which the bias is generally small over N. America. The RMSE is occasionally improved with CY47R1_NEWDEP as compared to CY45R1. This increase in simulated biomass burning aerosols could be caused by changes in deposition, as there are no changes in the GFAS emissions used between the three experiments. It is very likely that the use of injection heights for biomass burning emissions in the two CY47R1 experiments also play a role.

25 Over Africa, the bias of CY45R1 is smaller than over other regions; CY47R1 shows a larger negative bias, which is in turn reduced by CY47R1_NEWDEP. Besides other changes, the implementation of the new dust emission scheme probably plays a significant role in the changes of the skill scores over Africa. The RMSE of simulated AOD at 500nm is generally improved as compared to CY45R1, more so with CY47R1_NEWDEP. There is little difference between the two CY47R1 experiments over China; the CY45R1 experiment shows a significant positiv bias after August 2017; the bias is generally quite small with

30 the two CY47R1 experiments, and RMSE is generally improved, sometimes significantly: for the September-December 2017 period, it is nearly halved. Finally, CY45R1 displays a significant low bias over India, of 0.2 in average. This bias is more than halved with the two CY47R1 experiments. The impact on RMSE is mixed: most of time improved, but at times degraded, such as in May-June 2017.
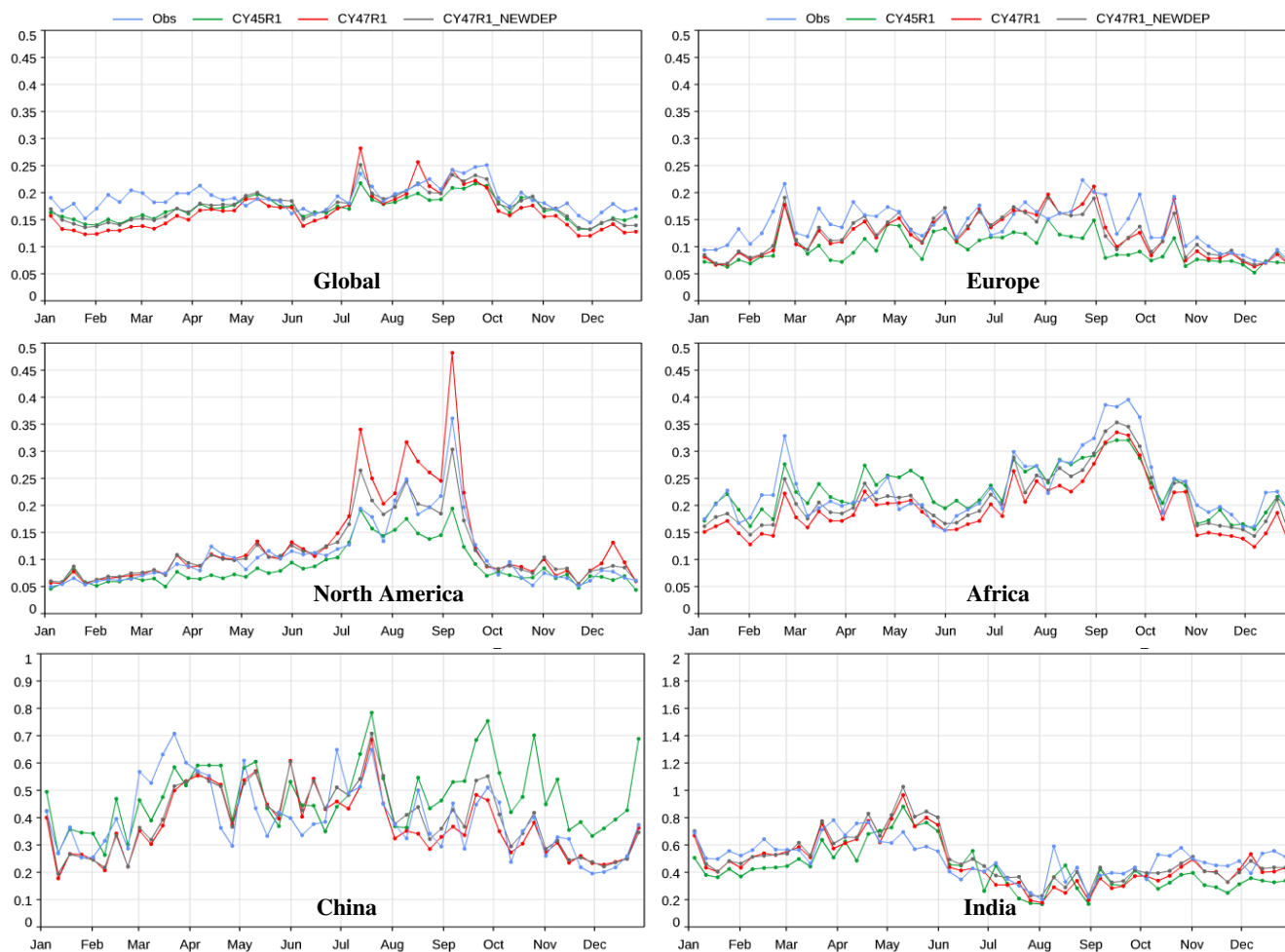
**Figure 13.** Global (top left) and regional simulated vs observed level 2 AOD at 500nm from AERONET, averaged over 7 days.

## 7.2 Evaluation against remote sensing products

### 7.2.1 AOD

Sogacheva et al. (2020) provide a new monthly product of merged AOD at 550nm, which combines the retrievals from a wide variety of remote sensors together with AERONET data. In order to assess the relative error of the simulated AOD at 550nm as compared to this product, the Fractional Gross Error (FGE) is used, so that the errors of the model in simulating relatively low values are not overlooked as compared to the larger errors that occur in regions where AOD is usually higher, such as over deserts and biomass burning regions. The FGE varies between 0 (best) and 2 (worst), and is defined for a population of N
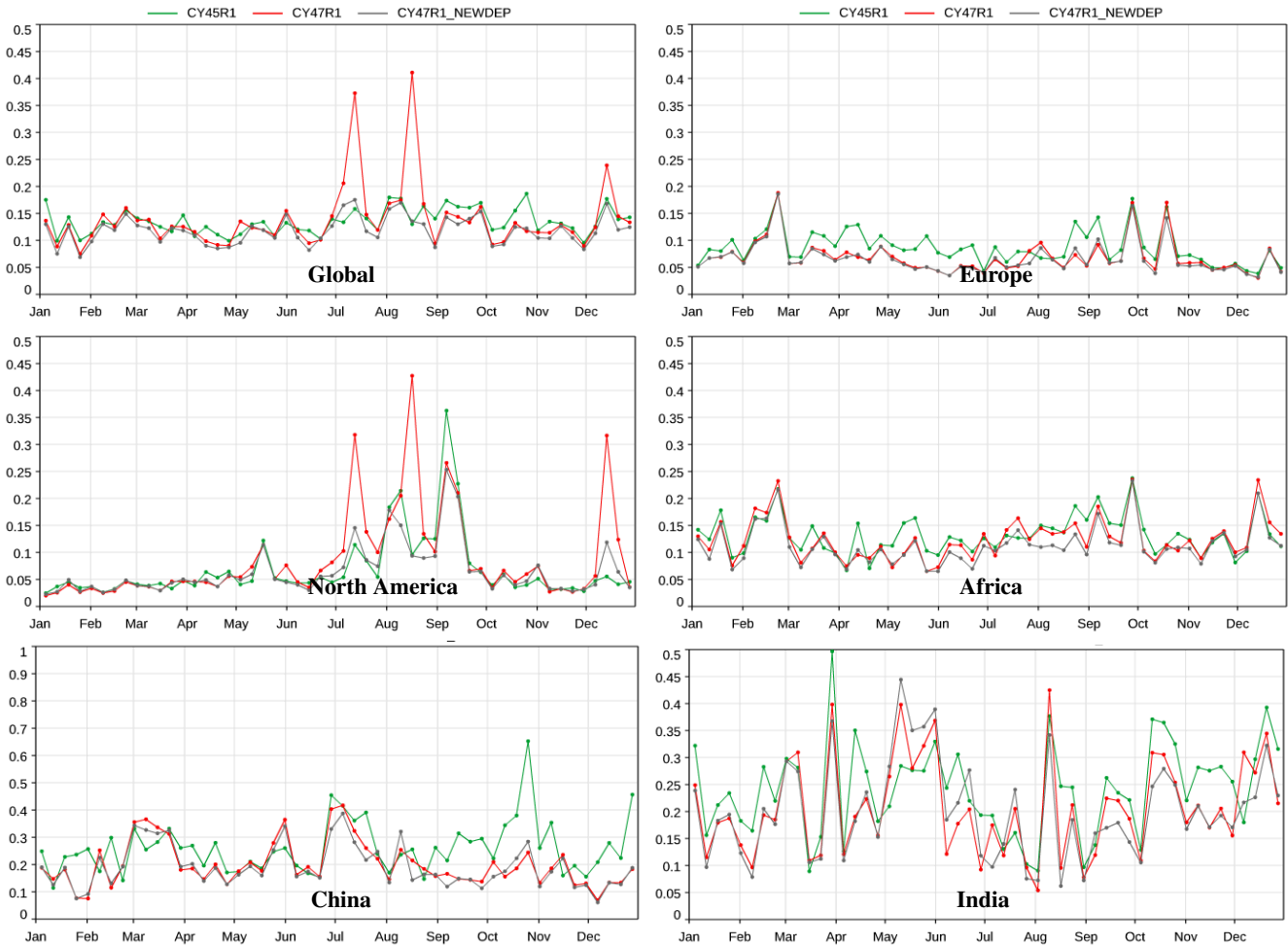
**Figure 14.** RMSE of simulated AOD at 500nm against Global (top left) and regionallevel 2 AOD from AERONET

forecasts $f_i$ and observations $o_i$ as:

$$FGE = \frac{2}{N} \sum_i \left| \frac{f_i - o_i}{f_i + o_i} \right| \tag{22}$$

Figure 15 shows collocated retrieved and simulated AOD at 550nm together with the fractional gross error of the simulated AOD. Over most oceans, CY45R1 is generally the closest to the merged AOD product, but the changes in wet and dry depo-

5   sition of CY47R1_NEWDEP bring a significant increase in simulated AOD as compared to CY47R1. The improved skill of the new sea-salt aerosol emission schemes shows in the FGE plots, which are significantly over most of oceans with CY47R1, and even more so with CY47R1_NEWDEP, as compared to CY45R1. Over most regions, the FGE of CY47R1_NEWDEP is lower than CY47R1. The decrease in FGE between CY45R1 and CY47R1 is not general: it concerns most of Europe, China,

Canada and Russia, a majority of oceans, Western Sahara. A few areas show a degradation in FGE: parts of Eastern Sahara, Indonesia and central Pacific.

### 7.2.2 Dust deposition

Observations of dust deposition are relatively sparse. Some are available over a few sites over the Western Mediterranean as
5 described in Vincent et al. (2016), or those collected at the Izana Global Atmospheric Watch Observatory in the Canary Islands by Waza et al. (2019). Here, we use the climatological dust deposition product from H. Yu (Yu et al. (2019)), as derived from remote sensing dust AOD. This product is based on several assumptions, such as a constant dust mass extinction, which probably don't always hold true. As such, it should be used for a qualitative rather than a quantitative assessment. It nevertheless provides an invaluable estimate of the total (dry + wet) dust deposition over the Atlantic. Figure 16 shows a comparison of this
10 climatological dust deposition against values simulated by a long cycle 47R1 cycling forecast (ie without data assimilation) experiment, which uses a configuration similar to CY47R1_NEWDUST. Overall, despite a local underestimation of the simulated dust deposition, the retrieved and simulated values match very well, which is a good indicator that IFS-AER manages to capture relatively well the climatological deposition of dust.

### 7.3 Evaluation against PM2.5 observations

15 PM2.5 is a key product provided by the global CAMS service: as such its evaluation is of special importance. Observed PM2.5 has been gathered from three geographical areas: Europe, North America and China. Over China, the site classification (rural or urban; background or traffic) is not known, so that the statistics probably include many sites that are not really suitable for comparison against simulations by a global model with a relatively coarse horizontal resolution.

Over the background rural stations of Europe, PM2.5 simulated by CY45R1 displayed a significant low bias, of 2-5 μg/m$^3$ in
20 general but reaching more than 10 μg/m$^3$ in January-February 2017. This period of the year 2017 witnessed a severe cold wave across much of Europe, which was probably associated with higher levels of residential wood burning and thus anthropogenic aerosol emissions. This kind of impact of meteorological parameters on emissions is currently not taken into account. The negative bias over Europe by CY45R1 is significantly improved by the two CY47R1 experiments, which simulated PM2.5 2-3 μg/m$^3$ than CY45R1 in winter months. The low bias in January and February 2017 is decreased by CY47R1 but far from
25 eliminated. CY47R1_NEWDEP is generally close to CY47R1, except in August and mid-October 2017. The mid-October 2017 spike in PM2.5 is associated with the large fires that struck Portugal then; the RMSE of CY47R1_NEWDEP is much lower than CY47R1 then, which shows that the new deposition options have a beneficial impact on the skill of simulated biomass burning plumes. Generally speaking, the RMSE of CY47R1 is much better than that of CY45R1, with a larger relative improvement in summer when the error is more than halved at times.

30 The overall picture is slightly different over the background rural stations of North America, where the simulated PM2.5 by CY45R1 shows little bias in winter months, but a significant positve bias of 2-3 μg/m$^3$ on average during summer months. As in Europe, the simulated PM2.5 is generally lower with the CY47R1 experiments, by 1-2 μg/m$^3$ in general but more during summer. This results is a small negative bias of 1-2 μg/m$^3$ with CY47R1 from January to April 2017, and a generally small bias

in the remaining months. The difference between CY47R1 and CY47R1_NEWDEP is mainly significant during summer, when CY47R1_NEWDEP is generally lower than CY47R1, and probably associated with the biomassburning aerosols. A spike in simulated PM2.5 in early September 2017 with CY47R1 is associated with fire events then; the significant positive bias of simulated PM2.5 by CY47R1 during this event is much improved by CY47R1_NEWDEP: as already noted over Europe, it

5   seems that CY47R1_NEWDEP generally improves the skill of the model in simulating PM from fire events. The RMSE of simulated PM2.5 is, as over Europe, significantly improved by the two CY47R1 experiments, for all months.

Over China, CY45R1 overestimates simulated PM2.5 constantly, and by a large margin, from 20 μg/m$^3$ to 40-60 μg/m$^3$ from September to December 2017. On average, the simulated PM2.5 is twice higher than the averaged observations. The very high positive bias is significantly reduced by CY47R1, for which the positive bias doesn't exceed 20 μg/m$^3$, and further reduced by

10   5-10 μg/m$^3$ in winter months by CY47R1_NEWDEP. In the end, CY47R1_NEWDEP shows little bias from January to April 2017, a significant positive bias of 10-20 μg/m$^3$ from May to October, and a smaller bias for the rest of 2017. Associated with this large improvement in bias is a decrease of RMSE with CY47R1 and even more with CY47R1_NEWDEP. For the whole of 2017, the RMSE of CY47R1_NEWDEP is nearly three times lower than that over CY45R1. The absolute value is still high, at 30 μg/m$^3$ on average, but this could also reflect the fact that many traffic stations are included in this dataset, for which there

15   is a high representativity error when comparing against global forecasts at a 50km horizontal resolution.

### 7.4   Evaluation against surface concentration observations

#### 7.4.1   Nitrate

The sum of the simulated nitrate surface concentration from gas-particle partitioning and from heterogeneous reactions is compared against observations from the CASTNET and EMEP networks in Figure 18. In general, over the considered re-

20   gions, nitrate from gas-particle partitioning is simulated to be much more abundant at surface than nitrate from heterogeneous reactions. The experiment CY47R1_NEWDEP is not shown because the simulated values differ relatively little from those simulated by CY47R1. Over the U.S., the simulated surface concentration of nitrate is significantly higher than observations. Over much of Eastern U.S., the simulated values vary between 2 and 4 μg/m$^3$ on average, while the observed values are generally in the range of 1-2 μg/m$^3$. The simulated values are also significantly overestimated over large parts of Europe, with averaged

25   reaching 3-6 μg/m$^3$ against obsreved values of 3-4 μg/m$^3$ in general. This significant overestimation is a quite frequent feature of global models: it has been noted in GEOS-CHEM (Luo et al., 2019) and GFDL (Paulot et al., 2016) and also in the Met Office Unified Model (Jones et al., 2021), in which the same nitrate scheme as IFS-AER has been adapted. A number of factors can participate to this overestimation: too high particle production as compared to gas phase, which is likely over Europe where the simulated nitric acid surface concentration is much lower than observed; overestimation in the emissions/burden of gaseous

30   precursors of nitric acid; underestimation of the sinks. Following Paulot et al. (2016), simulations that apply the dry deposition velocity of nitric acid to nitrate have been carried out and were shown to reduce significantly the positive bias of simulated nitrate at surface. However these developments are recent and have not yet been included in operational IFS-AER.

### 7.4.2 Ammonium

As for nitrate, the simulated surface concentration of ammonium is generally significantly overestimated over the U.S. and Europe, as shown by Figure 19. This comparison is not exactly representative, as ammonium from ammonium sulphate is part of the reported observations, while the ammonium species include only ammonium from ammonium nitrte. Over Europe, ammonia is also very much overestimated, which is not the case of the U.S.. At least over Europe, it is possible that the overestimation of ammonium can be partly explained by a too high ammonia burden, either from too high emissions or too little deposition.

### 7.4.3 Organic carbon

The IMPROVE networks disseminates observations of the surface concentration of organic carbon included in PM2.5 over the U.S.. Organic carbon has been derived from the hydrophilic and hydrophobic components of simulated organic matter, by applying a 2.3 OM:OC ratio for the hydrophilic fraction, and a 1.4 ratio for the hydrophobic one. These values are used by the EPA to convert organic matter from CAMS products into organic carbon (C. Hogrefe, personal communication). This is a strong assumption, as these ratios are known to vary a lot depending on the aerosol source, transport, aging, etc.. El-Zanan et al. (2005) found a mean value of 2.07 for the OM:OC ratio over all IMPROVE sites, using data from 1988 to 2003, which is consistent with our values. The fraction of organic carbon in PM2.5 is derived from the surface concentration of organic carbon by applying a 0.7 factor, consistent with the PM2.5 formula used in IFS-AER, which relates to the assumed size distribution of the organic matter species.

Figure 20 shows simulated and observed organic carbon in PM2.5 for the three CY45R1, CY47R1 and CY47R1_NEWDEP experiments. The simulated values are very much overestimated with CY45R1, reaching 4-6 μg/m$^3$ on average in the south-east, while observations are in the range of 2 μg/m$^3$. In the west, spikes of simulated very high values, above 10 μg/m$^3$ correspond to fire events. There are no such spikes in the observed values. The simulated surface concentration of OC in PM2.5 is significantly reduced with CY47R1. As the emissions are the same, this can be explained by the use of injection heights for biomass burning emissions, and possibly the by the impact of the new scavenging scheme. Despite this decrease, the simulated values are still generally higher than the observations, at 3-5 μg/m$^3$ in the south-east for example. The spikes associated with fires are smaller in extent but still present. These spikes are largely reduced with CY47R1_NEWDEP, which is consistent with the conclusions from the evaluation against PM2.5 observations, where a strong impact of the new deposition options on simulated PM2.5 from biomass burning origin was noted. CY47R1_NEWDEP bring a further significant decrease in simulated surface organic carbon in PM2.5 over the whole of the U.S. Despite this, the simulated values are still generally higher than the observations. This could be explained by the fact that secondary organic aerosols, which represent a large fraction of the emissions of organic matter, are released at the surface, while in reality they are produced by reactions aloft.

# 8 Conclusions

IFS-AER represents a simple modelling approach where many processes are either overlooked or heavily simplified, in order to meet the computational cost constraints associated with a global operational production. However, thanks to continuous development and evaluation, as well as drawing on the deeper integration with the global chemistry component of the IFS,

5  the skill of IFS-AER in simulating AOD and PM has been increasing significantly as compared to results obtained with cycle CY45R1. The evaluation is more and more diverse, making use of a large amount of ground and remote sensing datasets, which allows for a more detailed diagnostic of the shortcomings of IFS-AER. Despite an improved skill in simulating many aspects and aerosol species, a significant overestimation in simulated nitrate, ammonium and organic carbon at surface has been noted. Work is ongoing to address these issues. this include the future specific treatment of secondary organic aerosols with the

10  implementation of a new species with anthropogenic and biogenic components, with a strong coupling to the global chemistry which will represent the life cycle of the secondary organic precursors and provide the production rates of secondary organic aerosols. Finally, a more complex gas-particle partitioning scheme, EQSAM4Clim (Metzger et al. (2016)) is in the process of being implemented, with the hope of improving the representation of gas-particle partitioning processes in IFS-AER. In the longer term, the implementation of EQSAM4Clim could also help in improving the representation of water uptake and aerosol

15  aging in IFS-AER.

*Code availability.*

Model codes developed at ECMWF are the intellectual property of ECMWF and its member states, and therefore the IFS code is not publicly available. ECMWF member-state weather services and their approved partners will get access granted. Access to an open version of the IFS code (OpenIFS) that includes cycle CY43R3 IFS-AER may be obtained from ECMWF

20  under an OpenIFS licence. More details at https://confluence.ecmwf.int/display/OIFS/About+OpenIFS.

*Author contributions.* SR drafted the paper; SR, ZK, VH and JF maintain and carry out developments on IFS-AER; PN and MM contributed to the desert dust and sea-salt parameterizations, VH to the coupling to IFS-CB05. MA, RE, VHP contributed to drafting and revising this article.

*Acknowledgements.* This work is supported by the Copernicus Atmospheric Monitoring Services (CAMS) programme managed by ECMWF

25  on behalf of the European Commission. A large number of observational datasets have been used in this work; the authors would like to thank all the actors that created and made public these datasets: NASA (MODIS, AERONET), the European Environment Agency (airbase), the Airnow network and the United States Environmental Protection Agency (EPA for the CASTNET and IMPROVE data), the Finish Meteorological Institute (FMI, merged AOD product), the national observatory of Athens (MIDAS product). We acknowledge the provision

of Chinese PM2.5 data by Bas Mijling (KNMI) as acquired as part of the MarcoPolo-Panda project (http://www.marcopolo-panda.eu<http://www.marcopolo-panda.eu)

# References

Agustí-Panareda, A., Massart, S., Chevallier, F., Boussetta, S., Balsamo, G., Beljaars, A., Ciais, P., Deutscher, N. M., Engelen, R., Jones, L., Kivi, R., Paris, J.-D., Peuch, V.-H., Sherlock, V., Vermeulen, A. T., Wennberg, P. O., and Wunch, D.: Forecasting global atmospheric $CO_2$, Atmos. Chem. Phys., 14, 11 959–11 983, 2014.

Albert, M. F. M. A., Anguelova, M. D., Manders, A. M. M., Schaap, M., and de Leeuw, G.: Parameterization of oceanic whitecap fraction based on satellite observations, Atmos. Chem. Phys., 16, 13 725–13 751, 2016.

Anguelova, M. D. and Webster, F.: Whitecap coverage from satellite measurements: A first step toward modeling the variability of oceanic whitecaps, J. Geophys. Res, 111, C03 017, 2006.

Benedetti, A., Morcrette, J.-J., Boucher, O., Dethof, A., Engelen, R., Fisher, M., Flentje, H., Huneeus, N., Jones, L., Kaiser, J., et al.: Aerosol analysis and forecast in the European centre for medium-range weather forecasts integrated forecast system: 2. Data assimilation, Journal of Geophysical Research: Atmospheres (1984–2012), 114, 2009.

Bian, H., Chin, M., Hauglustaine, D. A., Schulz, M., Myhre, G., Bauer, S. E., Lund, M. T., Karydis, V. A., Kucsera, T. L., Pan, X., Pozzer, A., Skeie, R. B., Steenrod, S. D., Sudo, K., Tsigaridis, K., Tsimpidi, A. P., and Tsyro, S. G.: Investigation of global particulate nitrate from the AeroCom phase III experiment, Atmos. Chem. Phys., 17, 12 911–12 940, 2017.

Boucher, O., Pham, M., and Venkataraman, C.: Simulation of the atmospheric sulfur cycle in the Laboratoire de Meteorologie Dynamique general circulation model: Model description, model evaluation, and global and European budgets, Note Scientifique de l'IPSL, 23, 27 pp., 2002.

Bourgeois, Q. and Bey, I.: Pollution transport efficiency toward the Arctic: Sensitivity to aerosol scavenging and source regions, J. Geophys. Res, 116, D08 213, 2011.

Croft, B., Lohmann, U., Martin, R. V., Stier, P., Wurzler, S., Feichter, J., Posselt, R., and Ferrachat, S.: Aerosol size-dependent below-cloud scavenging by rain and snow in the ECHAM5-HAM, Atmos. Chem. Phys., 9, 4653–4675, 2009.

de Bruine, M., Krol, M., van Noije, T., Le Sager, P., and Röckmann, T.: The impact of precipitation evaporation on the atmospheric aerosol distribution in EC-Earth v3.2.0, Geosci. Model Dev., 11, 1443–1465, 2018.

El-Zanan, H., Lowenthal, D., Zielinska, B., Chow, J., and Kumar, N.: Determination of the organic aerosol mass to organic carbon ratio in IMPROVE samples, Chemosphere, 60, 485–498, 2005.

Engelen, R. J., Serrar, S., and Chevallier, F.: Four-dimensional data assimilation of atmospheric $CO_2$ using AIRS observations, Journal of Geophysical Research: Atmospheres, 114, https://doi.org/10.1029/2008JD010739, https://agupubs.onlinelibrary.wiley.com/doi/abs/10.1029/2008JD010739, 2009.

Fecan, F., Marticorena, B., and Bergametti, G.: Parameterization of the increase of aeolian erosion threshold wind friction velocity due to soil moisture for arid and semi-arid areas, Ann. Geophys., 17, 149–157, 1999.

Flemming, J., Inness, A., Flentje, H., Huijnen, V. andMoinat, P., Schultz, M. G., and Stein, O.: Coupling global chemistry transport models to ECMWF's integrated forecast system, Geoscientific Model Development, 2, 253–265, 2009.

Flemming, J., Huijnen, V., Arteta, J., Bechtold, P., Beljaars, A., Blechschmidt, A.-M., Diamantakis, M., Engelen, R. J., Gaudel, A., Inness, A., Jones, L., Josse, B., Katragkou, E., Marecal, V., Peuch, V.-H., Richter, A., Schultz, M. G., Stein, O., and Tsikerdekis, A.: Tropospheric chemistry in the Integrated Forecasting System of ECMWF, Geosci. Model Dev., 8, 975–1003, 2015.

Gilette, D. A.: Environmental Factors Affecting Dust Emission by Wind Erosion, 1979.

Ginoux, P., Chin, M., Tegen, I., Prospero, J. M., Holben, B., Dubovik, O., and Lin, S.-J.: Sources and distributions of dust aerosols simulated with the GOCART model, Journal of Geophysical Research: Atmospheres, 106, 20 255–20 273, 2001.

Ginoux, P., Prospero, J. M., Gill, T. E., Hsu, N. C., and Zhao, M.: Global-scale attribution of anthropogenic and natural dust sources and their emission rates based on MODIS Deep Blue aerosol products, Reviews of Geophysics, 50, https://doi.org/10.1029/2012RG000388, https://agupubs.onlinelibrary.wiley.com/doi/abs/10.1029/2012RG000388, 2012.

Giorgi, F. and Chameides, W. L.: Rainout lifetimes of highly soluble aerosols and gases as inferred from simulations with a general circulation model, J. Geophys. Res., 91, 367–376, 1986.

Gkikas, A., Proestakis, E., Amiridis, V., Kazadzis, S., Di Tomaso, E., Tsekeri, A., Marinou, E., Hatzianastassiou, N., and Pérez García-Pando, C.: ModIs Dust AeroSol (MIDAS): a global fine-resolution dust optical depth data set, Atmos. Meas. Tech., 14, 309–334, 2020.

Gliß, J., Mortier, A., Schulz, M., Andrews, E., Balkanski, Y., Bauer, S. E., Benedictow, A. M. K., Bian, H., Checa-Garcia, R., Chin, M., Ginoux, P., Griesfeller, J. J., Heckel, A., Kipling, Z., Kirkevåg, A., Kokkola, H., Laj, P., Le Sager, P., Lund, M. T., Lund Myhre, C., Matsui, H., Myhre, G., Neubauer, D., van Noije, T., North, P., Olivié, D. J. L., Rémy, S., Sogacheva, L., Takemura, T., Tsigaridis, K., and Tsyro, S.: AeroCom phase III multi-model evaluation of the aerosol life cycle and optical properties using ground- and space-based remote sensing as well as surface in situ observations, Atmos. Chem. Phys., 21, 87–128, 2021.

Granier, C., Bessagnet, B., Bond, T., D'Angiola, A., v. d. Gon, H. D., Frost, G. J., Heil, A., Kaiser, J. W., Kinne, S., Klimont, Z., Kloster, S., Lamarque, J.-F., Liousse, C., Masui, T., Meleux, F., Mieville, A., Ohara, T., Raut, J.-C., Riahi, K., Schultz, M. G., Smith, S. J., Thomson, A., v. Aardenne, J., v. d. Werf, G. R., and v. Vuuren, D. P.: Evolution of anthropogenic and biomass burning emissions of air pollutants at global and regional scales during the 1980–2010 period, Climate Change, 109, 163–190, 2011.

Granier, C., Darras, S., Denier van der Gon, H., Doubalova, J., Elguindi, N., Galle, B., Gauss, M., Guevara, M., Jalkanen, J.-P., Kuenen, J., Liousse, C., Quack, B., Simpson, D., and Sindelarova, K.: The Copernicus Atmosphere Monitoring Service global and regional emissions (April 2019 version), CAMS reports, https://doi.org/10.24380/d0bn-kx16, http://dx.doi.org/10.24380/d0bn-kx16, 2019.

Grythe, H., Ström, J., Krejci, R., Quinn, P., and Stohl, A.: A review of sea-spray aerosol source functions using a large global set of sea salt aerosol concentration measurements, Atmos. Chem. Phys., 14, 1277–1297, 2014.

Holben, B. N., Eck, T., Slutsker, I., Tanre, D., Buis, J., Setzer, A., Vermote, E., Reagan, J., Kaufman, Y., Nakajima, T., et al.: AERONET—A federated instrument network and data archive for aerosol characterization, Remote sensing of environment, 66, 1–16, 1998.

Hollingsworth, A., Engelen, R. J., Textor, C., Benedetti, A., Boucher, O., Chevallier, F., Dethof, A., Elbern, H., Eskes, H., Flemming, J., Granier, C., Kaiser, J. W., Morcrette, J.-J., Rayner, P., Peuch, V. H., Rouil, L., Schultz, M. G., Simmons, A. J., and Consortium, T. G.: Toward a Monitoring and Forecasting System For Atmospheric Composition: The GEMS Project, Bulletin of the American Meteorological Society, 89, 1147–1164, 2008.

Huijnen, V., Flemming, J., Chabrillat, S., Errera, Q., Christophe, Y., Blechschmidt, A.-M., Richter, A., and Eskes, H.: C-IFS-CB05-BASCOE: stratospheric chemistry in the Integrated Forecasting System of ECMWF, Geoscientific Model Development, 9, 3071–3091, 2016.

Inness, A., Baier, F., Benedetti, A., Bouarar, I., Chabrillat, S., Clark, H., Clerbaux, C., Coheur, P., Engelen, R. J., Errera, Q., Flemming, J., George, M., Granier, C., Hadji-Lazaro, J., Huijnen, V. andHurtmans, D., Jones, L., Kaiser, J. W., Kapsomenakis, J., Lefever, K., Leitão, J., Razinger, M., Richter, A., Schultz, M. G., Simmons, A. J., Suttie, M., Stein, O., Thépaut, J.-N., Thouret, V., Vrekoussis, M., and the MACC team: The MACC reanalysis: an 8 yr data set of atmospheric composition, Atmospheric Chemistry and Physics, 13, 4073–4109, 2013.

Inness, A., Ades, M., Agustí-Panareda, A., Barré, J., Benedictow, A., Blechschmidt, A.-M., Dominguez, J. J., Engelen, R., Eskes, H., Flemming, J., Huijnen, V., Jones, L., Kipling, Z., Massart, S., Parrington, M., Peuch, V.-H., Razinger, M., Remy, S., Schulz, M., , and Suttie, M.: The CAMS reanalysis of atmospheric composition, Atmospheric Chemistry and Physics, 19, 3515–3556, 2019.

Jaeglé, L., Quinn, P. K., Bates, T. S., Alexander, B., and Lin, J.-T.: Global distribution of sea salt aerosols: new constraints from in situ and remote sensing observations, Atmos. Chem. Phys., 11, 3137–3157, 2011.

Jones, A. C., Hill, A., Remy, S., Abraham, N. L., Dalvi, M., Hardacre, C., Hewitt, A. J., Johnson, B., Mulcahy, J. P., and Turnock, S. T.: Exploring the sensitivity of atmospheric nitrate concentrations to nitric acid uptake rate using the Met Office's Unified Model, Atmos. Chem. Phys., 21, in review, 2021.

Khan, T. and Perlinger, J. A.: Evaluation of five dry particle deposition parameterizations for incorporation into atmospheric transport models, Geoscientific Model Development, 10, 3861–3888, 2017.

Kok, J. F.: A scaling theory for the size distribution of emitted dust aerosols suggests climate models underestimate the size of the global dust cycle, Proceedings of the National Academy of Sciences, 108, 1016–1021, 2011.

Levy, R., Mattoo, S., Munchak, L., Remer, L., Sayer, A., Patadia, F., and Hsu, N.: The Collection 6 MODIS aerosol products over land and ocean, Atmospheric Measurement Techniques, 6, 2989, 2013.

Luo, G., Yu, F., and Schwab, J.: Revised treatment of wet scavenging processes dramatically improves GEOS-Chem 12.0.0 simulations of surface nitric acid, nitrate, and ammonium over the United States, Geosci. Model Dev., 12, 3439–3447, 2019.

Marticorena, B. and Bergametti, G.: Modeling the atmosphere dust cycle: 1. Design of a soil-derived dust emission scheme, J. Geophys. Res, 100, 16 415–16 430, 1995.

Metzger, S., Steil, B., Abdelkader, M., Klingmüller, K., Xu, L., Penner, J. E., Fountoukis, C., Nenes, A., and Lelieveld, J.: Aerosol water parameterisation: a single parameter framework, Atmos. Chem. Phys., 16, 7213–7237, 2016.

Michou, M., Nabat, P., and Saint-Martin, D.: Development and basic evaluation of a prognostic aerosol scheme (v1) in the CNRM Climate Model CNRM-CM6, Geoscientific Model Development, 8, 501–531, 2015.

Monahan, E. C. and Muircheartaigh, I. O.: Optimal power-law description of oceanic whitecap coverage dependence on wind speed, J. Phys. Oceanogr., 10, 2094–2099, 1980.

Monahan, E. C., Spiel, D. E., and Davidson, K. L.: A model of marine aerosol generation via whitecaps and wave disruption, in: Oceanic Whitecaps and Their Role in Air–Sea Exchange Processes, edited by Monahan, E. C. and MacNiocaill, G., pp. 167–174, D. Reidel, 1986.

Morcrette, J.-J., Boucher, O., Jones, L., Salmond, D., Bechtold, P., Beljaars, A., Benedetti, A., Bonet, A., Kaiser, J., Razinger, M., et al.: Aerosol analysis and forecast in the European Centre for medium-range weather forecasts integrated forecast system: Forward modeling, Journal of Geophysical Research: Atmospheres, 114, 2009.

Nabat, P., Solmon, F., Mallet, M., Kok, J., and Somot, S.: Dust emission size distribution impact on aerosol budget and radiative forcing over the Mediterranean region: a regional climate model approach, Atmos. Chem. Phys., 12, 10 545–10 567, 2012.

Paulot, F., Ginoux, P., Cooke, W. F., Donner, L. J., Fan, S., Lin, M.-Y., Mao, J., Naik, V., and Horowitz, L. W.: Sensitivity of nitrate aerosols to ammonia emissions and to nitrate chemistry: implications for present and future nitrate optical depth, Atmos. Chem. Phys., 16, 1459–1477, 2016.

Popp, T., De Leeuw, G., Bingen, C., Brühl, C., Capelle, V., Chedin, A., Clarisse, L., Dubovik, O., Grainger, R., Griesfeller, J., Heckel, A., Kinne, S., Klüser, L., Kosmale, M., Kolmonen, P., Lelli, L., Litvinov, P., Mei, L., North, P., Pinnock, S., Povey, A., Robert, C., Schulz, M., Sogacheva, L., Stebel, K., Stein Zweers, D., Thomas, G., Tilstra, L. G., Vandenbussche, S., Veefkind, P., Vountas, M., and Xue, Y.:

Development, Production and Evaluation of Aerosol Climate Data Records from European Satellite Observations (Aerosol_cci), Remote Sensing, 8, https://doi.org/10.3390/rs8050421, http://www.mdpi.com/2072-4292/8/5/421, 2016.

Reddy, M. S., Boucher, O., Bellouin, N., Schulz, M., Balkanski, Y., Dufresne, J.-L., and Pham, M.: Estimates of global multicomponent aerosol optical depth and direct radiative perturbation in the Laboratoire de Météorologie Dynamique general circulation model, J. Geo-

5    phys. Res., 110, D10S16, 2005.

Rémy, S., Veira, A., Paugam, R., Sofiev, M., Kaiser, J. W., Marenco, F., Burton, S. P., Benedetti, A., Engelen, R. J., Ferrare, R., and Hair, J. W.: Two global data sets of daily fire emission injection heights since 2003, Atmospheric Chemistry and Physics, 17, 2921–2942, 2017.

Rémy, S., Kipling, Z.and Flemming, J., Boucher, O., Nabat, P., Michou, M., Bozzo, A., Ades, M., Huijnen, V., Benedetti, A., Engelen, R., Peuch, V.-H., and Morcrette, J.-J.: Description and evaluation of the tropospheric aerosol scheme in the European Centre for Medium-

10   Range Weather Forecasts (ECMWF) Integrated Forecasting System (IFS-AER, cycle 45R1), Geosci. Model Dev., 12, 4627–4659, 2019.

Shangguan, W., Dai, Y., Duan, Q., Liu, B., and Yuan, H.: A global soil data set for earth system modeling, J. Adv. Model. Earth Syst., 6, 249–263, 2014.

Smirnov, A., Holben, B., Slutsker, I., Giles, D., McClain, S., Eck, T., Sakerin, S., Macke, A., Croot, P., Zibordi, G., Quinn, P., Sciare, J., Kinne, S., Harvey, M., Smyth, T., Piketh, S., Zielinski, G., Proshutinsky, A., Goes, J. I., Nelson, N. B., Larouche, P., Radionov, V. F.,

15   Goloub, P., Krishna Moorthy, K., Matarrese, R., Robertson, E., and Jourdin, F.: Maritime Aerosol Network as a component of Aerosol Robotic Network, J. Geophys. Res, 114, D06 204, 2009.

Sogacheva, L., Popp, T., Sayer, A. M., Dubovik, O., Garay, M. J., Heckel, A., Hsu, N. C., Jethva, H., Kahn, R. A., Kolmonen, P., Kosmale, M., de Leeuw, G., Levy, R. C., Litvinov, P., Lyapustin, A., North, P., Torres, O., and Arola, A.: Merging regional and global aerosol optical depth records from major available satellite products, Atmos. Chem. Phys., 20, 2031–2056, 2020.

20   Spracklen, D. V., Jimenez, J. L., Carslaw, K. S., Worsnop, D. R., Evans, M. J., Mann, G. W., Zhang, Q., Canagaratna, M. R., Allan, J., Coe, H., McFiggans, G., Rap, A., and Forster, P.: Aerosol mass spectrometer constraint on the global secondary organic aerosol budget, Atmos. Chem. Phys., 11, 12 109–12 136, 2011.

Vincent, J., Laurent, B., Losno, R., Bon Nguyen, E., Roullet, P., Sauvage, S., Chevaillier, S., Coddeville, P., Ouboulmane, N., di Sarra, A. G., Tovar-Sánchez, A., Sferlazzo, D., Massanet, A., Triquet, S., Morales Baquero, R., Fornier, M., Coursier, C., Desboeufs, K., Dulac, F., and

25   Bergametti, G.: Variability of mineral dust deposition in the western Mediterranean basin and south-east of France, Atmos. Chem. Phys., 16, 8749–8766, 2016.

Waza, A., Schneiders, K., May, J., Rodríguez, S., Epple, B., and Kandler, K.: Field comparison of dry deposition samplers for collection of atmospheric mineral dust: results from single-particle characterization, Atmos. Meas. Tech., 12, 6647–6665, 2019.

Yu, H., Tan, Q., Chin, M., Remer, L. A., Kahn, R. A., Bian, H., Dongchul, K., Zhibo, Z., Tianle, Y., Ali, O., Winker, D., Levy, R., Kalash-

30   nikova, O., Crepeau, L., Capelle, V., and Chédin, A.: Estimates of African dust deposition along the trans-Atlantic transit using the decadelong record of aerosol measurements from CALIOP, MODIS, MISR, and IASI, J. Geophys. Res, 124, 7975–7996, 2019.

Zender, C. S., Newman, D., and Torres, O.: Spatial heterogeneity in aeolian erodibility: Uniform, topographic, geomorphic, and hydrologic hypotheses, J. Geophys. Res, 108 (D17), 4543–4555, 2003.

Zhang, L. and He, Z.: Technical Note: An empirical algorithm estimating dry deposition velocity of fine, coarse and giant particles, Atmos.

35   Chem. Phys., 14, 3729–3727, 2014.

Zhang, L., Gong, S., Padro, J., and Barrie, L.: A size-segregated particle dry deposition scheme for an atmospheric aerosol module, Atmospheric Environment, 35, 549–560, https://doi.org/https://doi.org/10.1016/S1352-2310(00)00326-5, 2001.
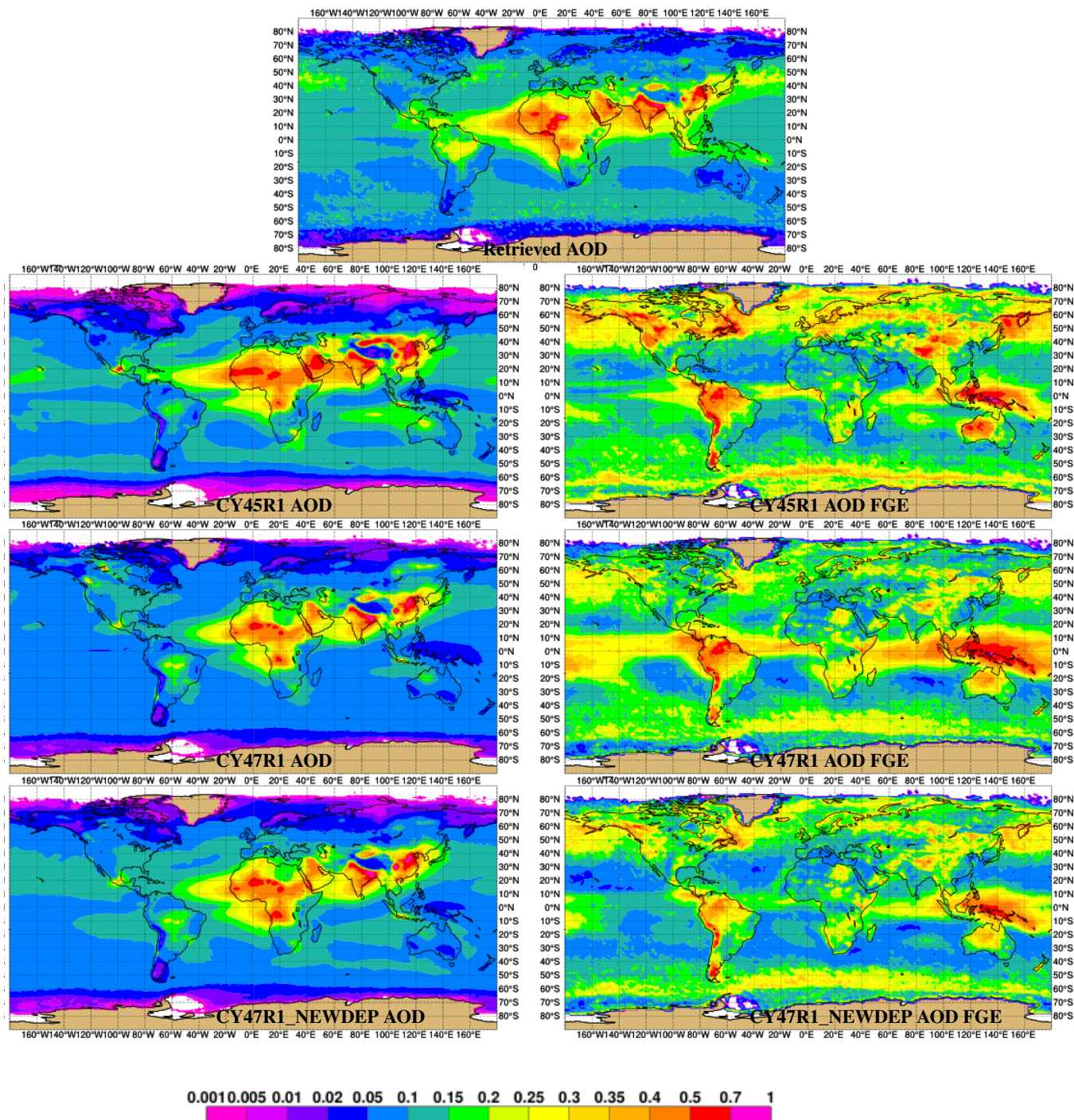
**Figure 15.** Top: February-December 2017 merged AOD at 550nm from Sogacheva et al. (2020). Left, collocated simulated AOD by CY45R1, CY47R1 and CY47R1_NEWDEP from top to bottom. Right, fractional gross error of simulated AOD against the merged AOD product, for CY45R1, CY47R1 and CY47R1_NEWDEP from top to bottom.
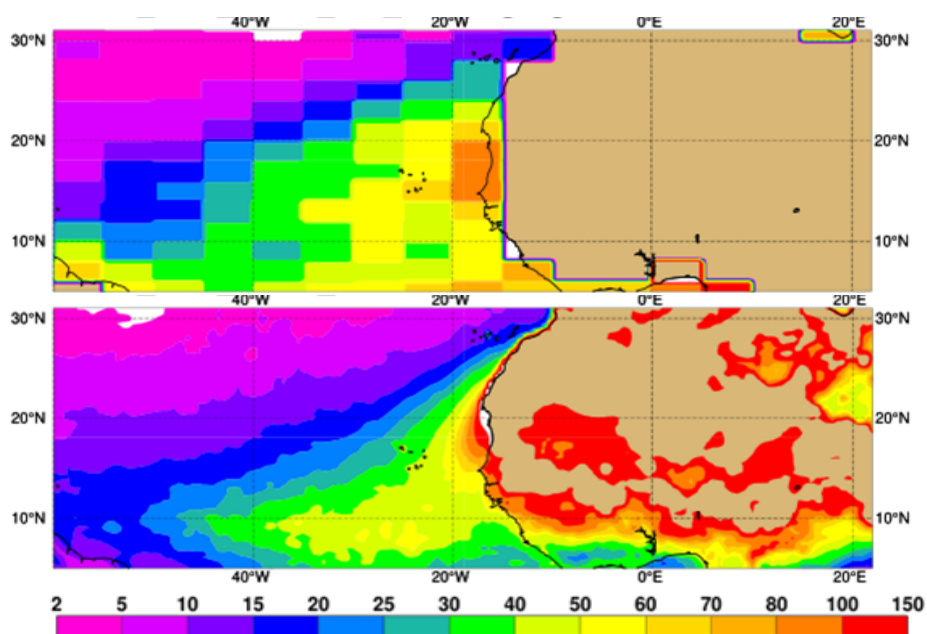
**Figure 16.** Top, 2007-2016 mean dust total deposition in mg/m²/day as estimated by MODIS; bottom, mean 2017-2019 mean dust total deposition as simulated by IFS-AER cycle 47R1 without data assimilation, in mg/m²/day.
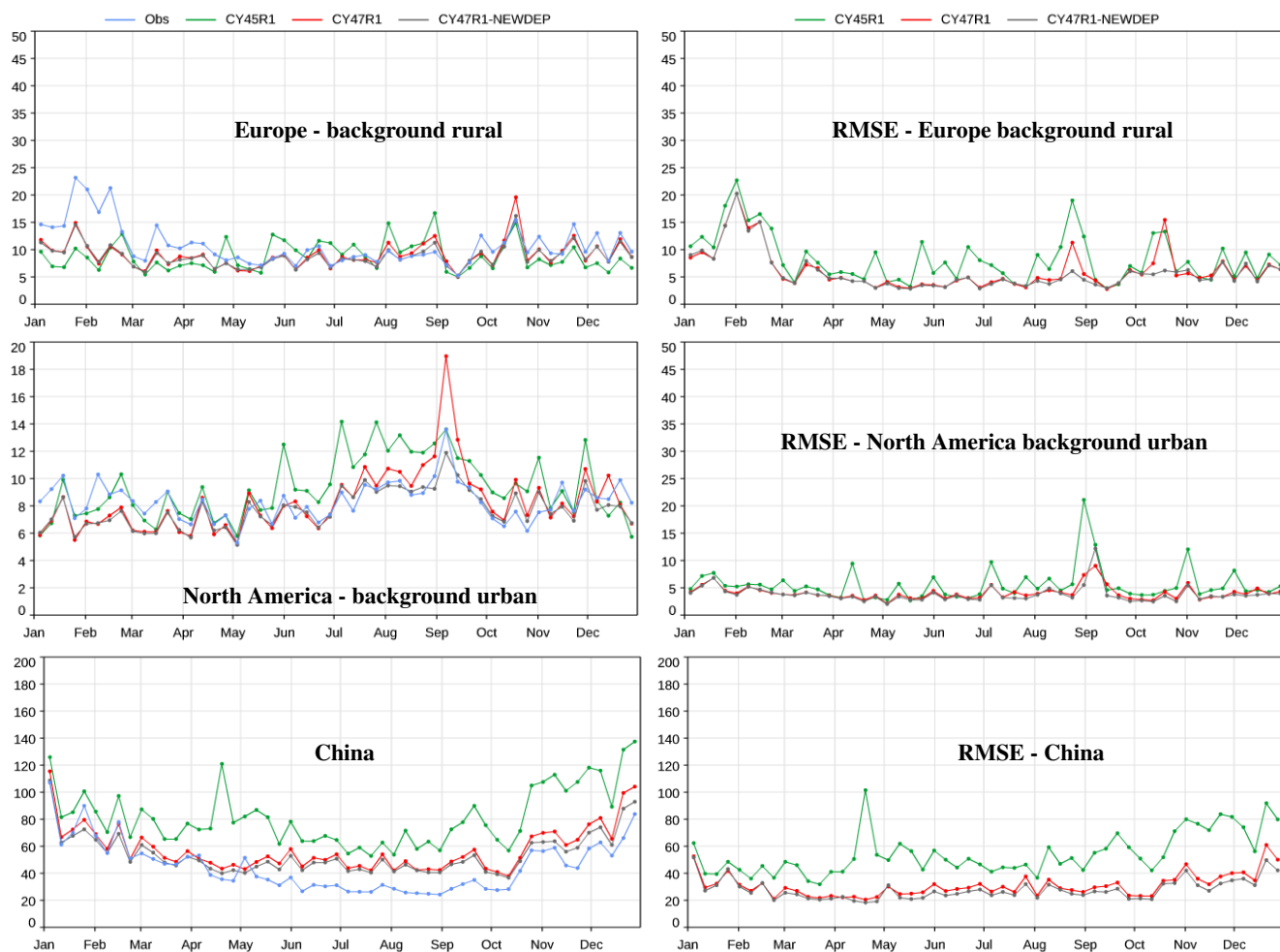
**Figure 17.** Left, observed and simulated weekly PM2.5 over Europe (background rural), North America (background urban) and China (all sites). Right, RMSE of simulated PM2.5 against observations.
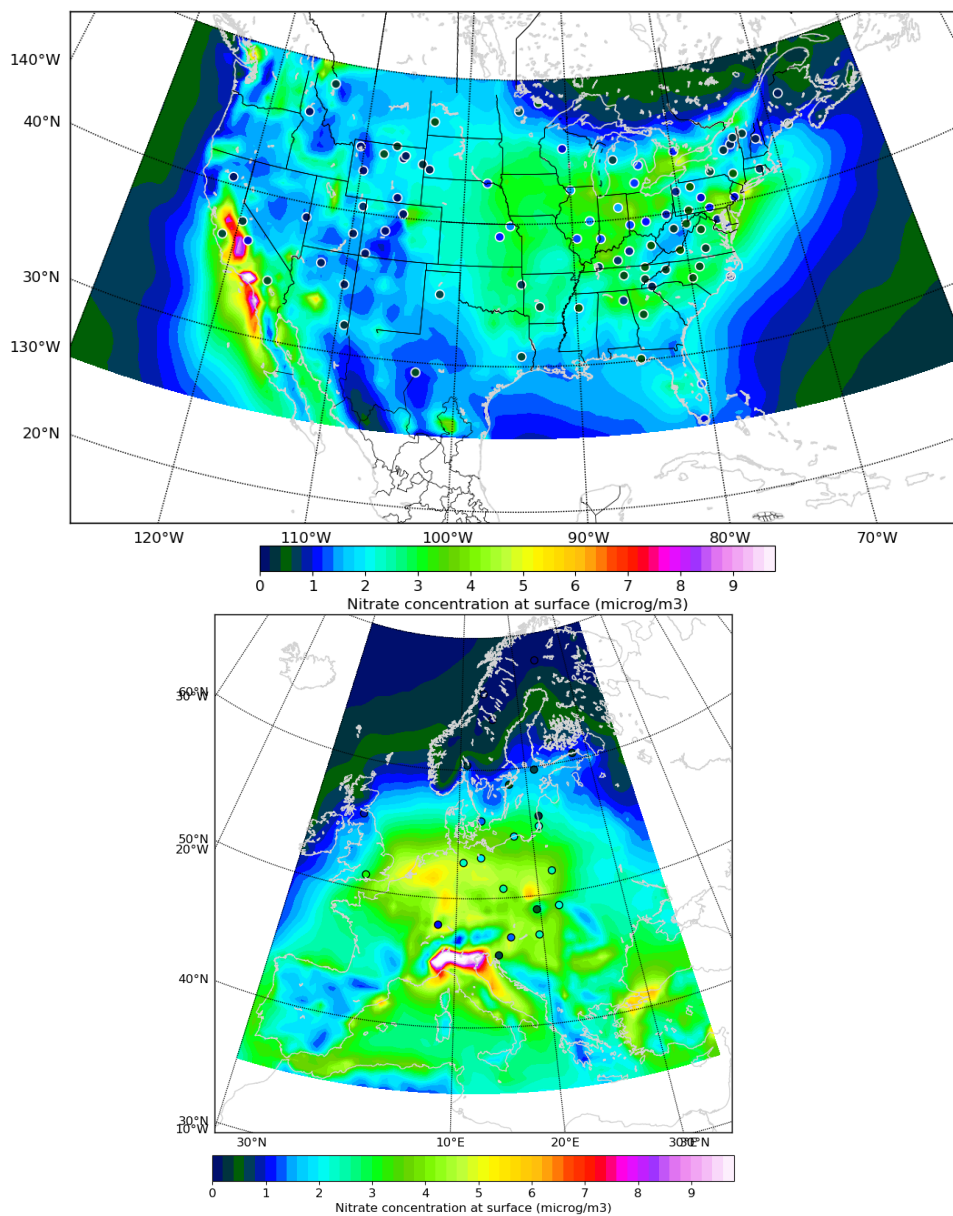
**Figure 18.** February-December 2017 surface nitrate concentration in $\mu g/m^3$ simulated by IFS-AER CY47R1 against yearly average from the CASTNET and the EMEP networks, as shown in black circles. Please note the different scale between the two panels.
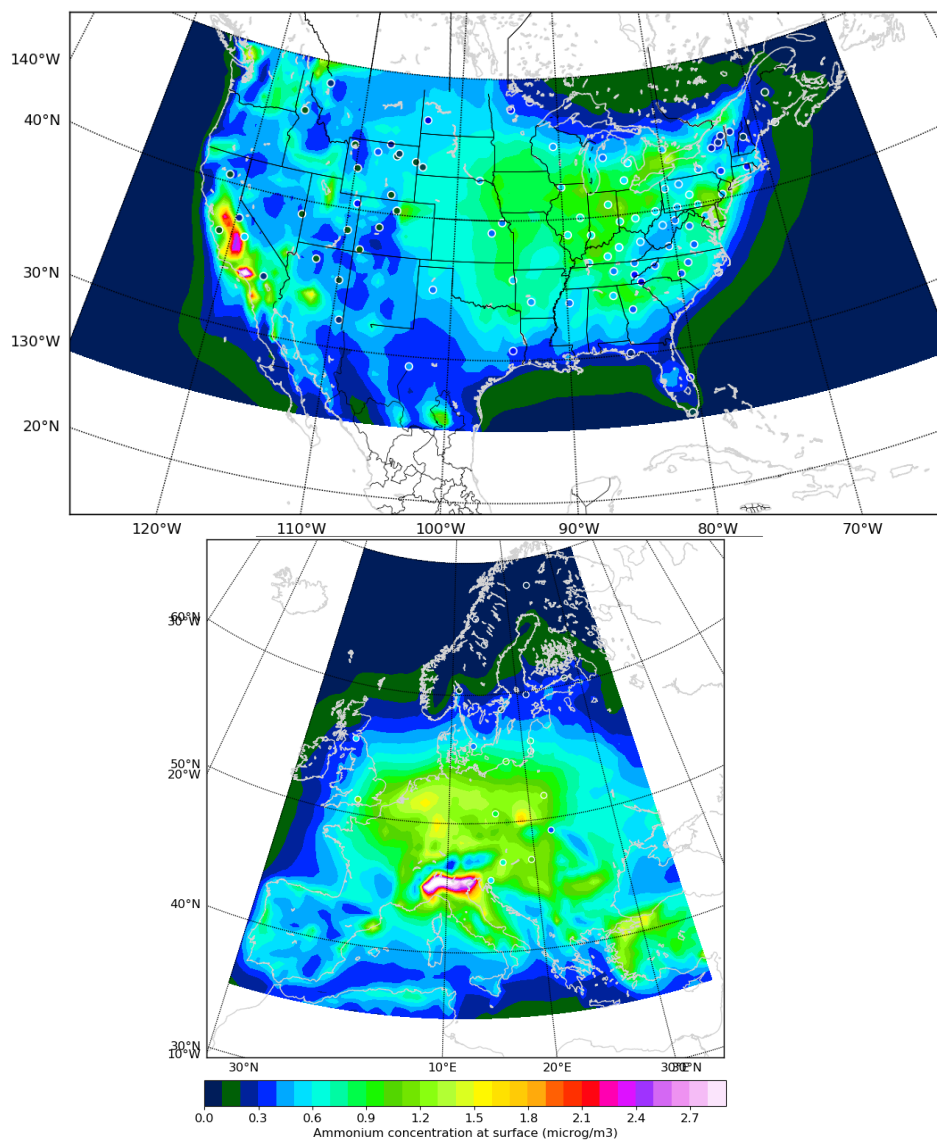
**Figure 19.** February-December 2017 surface ammonium concentration in $\mu g/m^3$ simulated by IFS-AER CY47R1 against yearly average from the CASTNET and the EMEP networks, as shown in black circles.
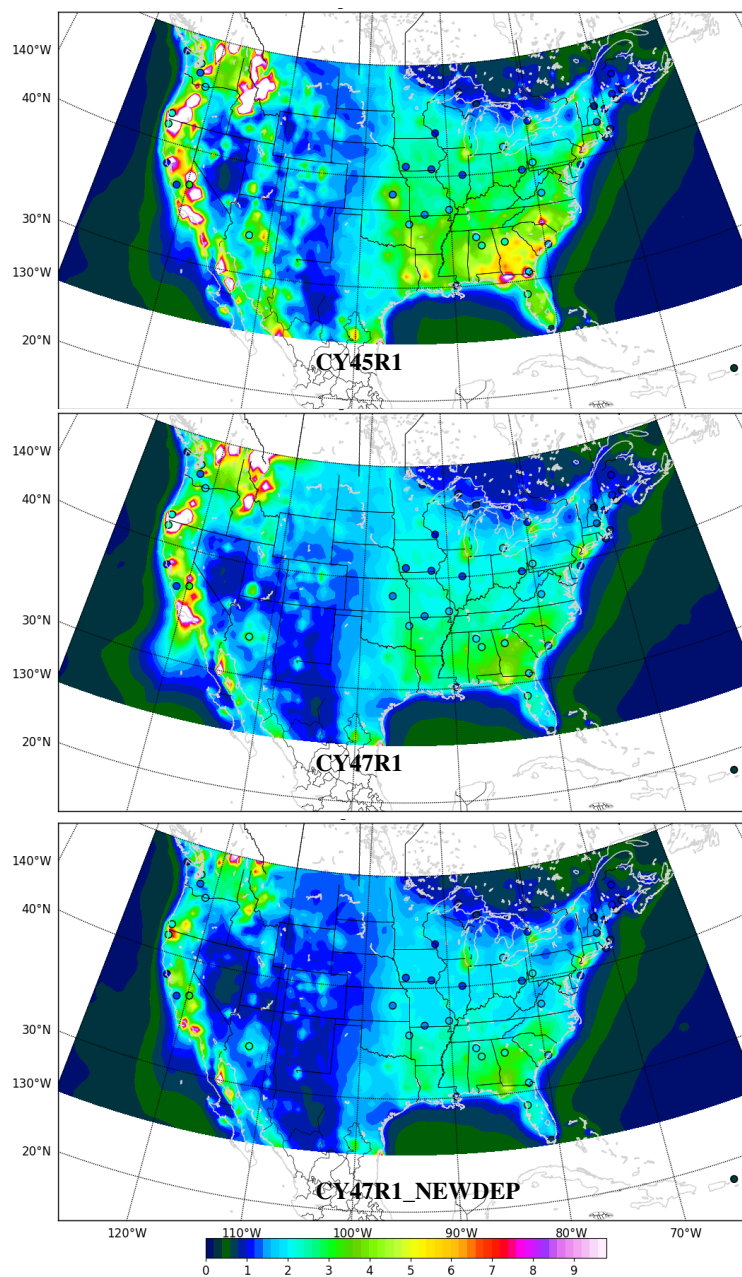
**Figure 20.** February-December 2017 surface ammonium concentration in $\mu g/m^3$ simulated by IFS-AER CY47R1 against yearly average from the CASTNET and the EMEP networks, as shown in black circles.